

Interpretation of coastal wind transfer functions with momentum balances derived from idealized numerical model simulations

Sung Yong Kim · Ganesh Gopalakrishnan · Aurelien Ponte

Received: 19 September 2013 / Accepted: 25 August 2014 / Published online: 20 September 2014
© Springer-Verlag Berlin Heidelberg 2014

Abstract The local wind-driven circulation off southern San Diego is addressed with two complementary statistical and dynamical frameworks based on observations and idealized numerical model simulations. The observations including surface currents from high-frequency radars, subsurface currents from a nearshore mooring, and wind records at a local wind station are analyzed with the idealized ocean model (MITgcm) simulations using realistic bottom topography and spatially uniform wind stress forcing. Statistically estimated anisotropic local wind transfer functions characterize the observed oceanic spectral response to wind stress separately in the x (east-west) and y (north-south) directions. We delineate the coastal circulation at three primary frequencies [low ($\sigma_L = 0.0767$ cycles per day (cpd)), diurnal ($\sigma_D = 1$ cpd), and inertial ($\sigma_f = 1.07$ cpd) frequencies] with the momentum budget equations and transfer functions. At low frequency, the magnitudes of transfer functions are enhanced near the coast, attributed

to geostrophic balance between wind-driven pressure gradients and the Coriolis force on currents. The response diminishes away from the coast, returning to the balance between frictional and Coriolis terms, as in the classic Ekman model. On the contrary, transfer functions in the near-inertial frequency band show reduced magnitudes near the coast primarily due to friction, but exhibits the enhanced seaward response as a result of the inertial resonance. The idealized model simulations forced by local wind stress can identify the influences of remote wind stress and the biases in the data-derived transfer functions.

Keywords Coastal wind-current system · Surface circulation · Subsurface circulation · Anisotropic transfer function · Anisotropic response function · Momentum balance · Statistical analysis · Inverse model

1 Introduction

The wind-driven circulation in the coastal regions has relatively energetic vertical currents and anisotropic and asymmetric horizontal responses as compared to the open ocean. The enhanced vertical velocity, concentrated at the coastal boundary due to the flows compensating the surface Ekman transports, plays a primary role in shelf ecosystem dynamics (e.g., Allen 1980; Brink 1991). The anisotropic and asymmetric wind-driven responses result from the complex combination of stratification (e.g., Allen et al. 1995; Weisberg et al. 2001), wind-driven pressure setup against the coast (e.g., Ekman 1905; Kim et al. 2010b), asymmetric bathymetry (e.g., Pringle 2002; Castelao and Barth 2005), non-constant eddy viscosity (e.g., Madsen 1977; Lentz 1995), and wave-driven currents, in particular, in the inner shelf (e.g., Lentz and Fewings 2012).

Responsible Editor: Pierre Lermusiaux

S. Y. Kim (✉)
Division of Ocean Systems Engineering, School of Mechanical, Aerospace, and Systems Engineering, Korea Advanced Institute of Science and Technology, 291 Daehak-ro, Yuseong-gu, Daejeon 305-701, Republic of Korea
e-mail: syongkim@kaist.ac.kr

G. Gopalakrishnan
Climate, Atmospheric Science and Physical Oceanography, Scripps Institution of Oceanography, 9500 Gilman Dr., La Jolla, CA 92093, USA
e-mail: ggopalakrishnan@ucsd.edu

A. Ponte
Laboratoire de Physique des Océans, IFREMER-CNRS-IRD-UBO, 29280, Plouzané, France
e-mail: aurelien.ponte@ifremer.fr

In the two-dimensional upwelling theory under the unstratified condition, the depth-integrated cross-shore transports are closed (e.g., Allen et al. 1995; Lentz 1995; Dever 1997). After the onset of upwelling-favorable winds, surface Ekman transports due to along-shore wind stress are dominantly compensated by the interior flow, then at steady-state, surface, Ekman transports are mainly balanced by the flows in the bottom boundary layer. In this transition, the frictional timescale (h/r , where h and r denote the water depth and bottom frictional coefficient, respectively) is a proxy to determine how flows in between bottom boundary layer and interior contribute to the cross-shore circulation. The surface pressure gradients in the cross-shore direction are built up by steady surface Ekman transports and simultaneously generate the geostrophic currents in the direction of wind stress. While the cross-shelf circulation on the midshelf is mainly driven by along-shelf wind stress, the inner shelf circulation where surface and bottom boundary layers merge can be governed by along-shore currents and topographic variation, and cross-shelf wind stress (e.g., Lentz et al. 1999; Austin and Lentz 2002). The downwind circulation in the inner shelf is associated with the fact that the timescale of vertical viscous diffusion (h^2/A_z , where A_z is the vertical diffusivity) is less than the rotational timescale ($1/f_c$, where f_c is the Coriolis frequency). In other words, it takes more time for the Coriolis force to be felt than for the momentum to penetrate from surface to bottom (e.g., Craig 1988; Lentz 2001; Shen and Evans 2001). Furthermore, a three-dimensional framework (e.g., momentum and mass balances) may be required to explain the whole wind-driven circulation (e.g., Brink et al. 1980; Davis and Bogden 1989). For example, the cross-shore geostrophic currents driven by along-shore pressure gradients can balance surface Ekman transports.

In observational studies of shelf circulation, it has been a difficult job to specify cross-shore currents in the momentum balance because either their order of magnitudes is similar to the uncertainty of observations or the Coriolis term becomes anomalously large compared to the other terms (e.g., Allen and Smith 1981; Pettigrew 1981; Lentz and Winant 1986; Lee et al. 1989; Lentz et al. 1999). Thus, the shelf circulation could be addressed with two-dimensional (only in the x and z spaces, where x and z indicate the cross-shore and vertical directions, respectively) decoupled momentum equations (e.g., Lentz et al. 1999). In this study, the three-dimensional ocean model simulations with realistic bottom topography and idealized wind forcing are designed to interpret the data-derived impulse response relationship and to reexamine the previously neglected circulation in the decoupled system (described above) and their roles in modulating the cross-shelf and along-shelf circulation (Section 5.1).

The statistical analysis using the transfer function (or impulse response function or Green's function) has a long history in the form of data analysis and signal processing in oceanographic and engineering communities (e.g., Emery and Thomson 1997; Oppenheim et al. 1998). The impulse response function characterizes the whole system by generating a unique response to a given impulse. Thus, the observed relationship between forcing and response allows us to identify the system. For instance, the oceanic system forced by wind stress (forcing) generates currents (response) and their statistical characterization describes the wind-current system. On the contrary, the primitive equations governing the flow also describe the system with the interlocked dynamical components. As a similar example, the momentum equations in a rotating frame of reference well represent the linear relationship between wind stress and currents as their primary relationship. These two approaches using transfer functions and governing equations delineate the system in different ways. Even though terms in each approach can correspond to each other, most of them may not be matched. Thus, the individual components of anisotropic transfer functions, which will be defined below, can be explained with terms in the momentum equations; however, it may not be guaranteed that all terms are explained.

Kim et al. (2009b) investigated the wind transfer functions derived from observations (using a single time series of local wind stress and spatially averaged surface currents) and from the Ekman model. The isotropic analysis assumes the response function to be independent of the wind direction by combining vector quantities into complex numbers ($\mathbf{u} = u + iv$ and $\boldsymbol{\tau} = \tau_x + i\tau_y$, where u and v are x - and y -directional current components and τ_x and τ_y are x - and y -directional wind stress, respectively). However, the anisotropic transfer functions allow isolating the individual directional wind responses, composed of four components. Kim et al. (2009b) extended the time-dependent Ekman theory by arbitrarily adding adjustment terms in the momentum equations which represent the coastline boundary effects by lumping together wind-forced pressure gradients, anisotropic stress divergence, and bottom topography in order to approximate the data-derived and model-derived transfer functions. However, a single term may not encapsulate all the relevant shelf dynamics.

Kim et al. (2010b) extended the previous wind-regression model with multiple wind-regression bases by examining the spatial maps of isotropic transfer functions at three frequencies (low, diurnal, and inertial frequencies) characterizing wind-current dynamics in the coastal regions. The magnitudes of isotropic transfer functions at diurnal and inertial frequencies are reduced near the coast, likely due to effects of coastline and bottom topography. Meanwhile,

the magnitude of low-frequency currents increases near the coast, which may be attributed to the local geostrophic balance between cross-shore pressure gradients against the coast and currents. However, isotropic transfer functions have limitations to isolate the wind response in individual directions. Furthermore, dynamical interpretations on those observational phenomena were not provided by Kim et al. (2009b, 2010b).

Kim (2014) compared the wind transfer functions of sea surface heights derived from observations and two-dimensional idealized model simulations. While the dynamical components in the along-shore direction were not included, the model could explain the geostrophic and frictional balances as a function of frequency and local depth. However, the spatial structures of pressure gradients and currents in the wind-driven coastal circulation were not resolved. Moreover, the observational resources and platforms were only limited to the tide gauge data.

A primary goal of this work is to interpret coastal wind transfer functions derived from observations and numerical model simulations, particularly, to understand the effects of the coast by isolating the ocean response to wind forcing at three primary frequencies [low ($\sigma_L = 0.0767$ cycles per day (cpd)), diurnal ($\sigma_D = 1$ cpd), and inertial ($\sigma_f = 1.07$ cpd) frequencies]. Observations of surface and subsurface currents obtained from high-frequency radars (HFRs) and acoustic Doppler current profiler (ADCP), respectively, and local winds are analyzed. The Massachusetts Institute of Technology general circulation model (MITgcm) simulations with realistic coastline and topography and spatially uniform wind stress forcing are also examined. Data-derived anisotropic wind transfer functions at three frequencies (e.g., low, diurnal, and inertial frequencies) are compared with those computed from the model simulations. This paper provides the horizontal maps related to wind-driven circulation (including cross-shore structure) derived purely from observations (e.g., spatial variation of wind-driven pressure gradients and near-inertial motions). Furthermore, all directional winds and currents are taken into account at three primary frequencies mentioned above. This paper is also designed to explain the anisotropic transfer functions with the known dynamics in the wind-current system and to identify the possible limits and biases imposed in the observations.

This paper consists of five sections. First, in situ observations and configuration of the numerical model are summarized (Section 2). Then, the definitions of anisotropic transfer functions for currents and sea surface heights (SSHs), the description of isotropic and anisotropic components, and the individual terms in the momentum budget equations are described (Section 3). The transfer functions at the surface and across the x - z sections are presented with dynamical

interpretations using the momentum balance (Section 4). The discussion and conclusion on those analyses follow in Sections 5 and 6, respectively.

2 Observations and idealized numerical model simulations

2.1 Observations of coastal currents and winds

Surface currents measured by three short-range HFRs [R1 (Point Loma), R2 (Border Park), and R3 (Coronado Islands) in Fig. 1] and subsurface currents from an ADCP deployed at 28 m depth (T in Fig. 1) off southern San Diego for two years (July 2007 to June 2009) are analyzed to estimate three-dimensional wind responses. The radial surface velocities measured by three HFRs are optimally interpolated to derive surface vector currents, covering an approximately $40 \text{ km} \times 40 \text{ km}$ coastal area off southern San Diego (e.g., Kim et al. 2008). Subsurface currents are collected as a part of continuous monitoring of the Tijuana River (TJR) plume. Both hourly surface and subsurface current time series are detided to remove the barotropic tidal variance at K_1 , O_1 , P_1 , S_2 , and M_2 frequencies, but not S_1 frequency, because S_1 tidal currents are considered very weak (e.g., Kim et al. 2010a). The spectral descriptions of in situ wind observations off southern San Diego have been discussed elsewhere (Kim et al. 2010b). The hourly wind data at the TJR Valley (W in Fig. 1) are converted into wind stress with the drag coefficient suggested by Yelland and Taylor (1996). The wind data at TJR and NDBC 46086 buoy (located at 32.5° N , 118° W , offshore of the study domain shown in Fig. 1) have weak coherence (0.2–0.4) in the low-frequency band ($\sigma < 0.4$ cycles per day (cpd)) and at the diurnal frequency. The wind harmonics at the NDBC 46086 buoy leads the TJR wind at all tested frequencies except for the diurnal frequency and its harmonics. The decorrelation length scales estimated from the Coupled Ocean/Atmosphere Mesoscale Prediction System (COAMPS) wind field (at 1.7 and 5.1 km model resolutions) off southern San Diego are in the range of 25 to 120 km (Appendix A and Fig. 13), which can justify the use of the TJR wind as the effective wind observation for the ADCP subsurface currents (Kim et al. 2010b).

As a result of the reduced spatial coverage of HFRs and bias in the radar beam patterns from 2007 to 2009, the wind and surface currents during a different two-year period (April 2003 to March 2005) are used to estimate surface transfer functions except for a comparison with the mooring. The wind forcing in two different time periods has a very similar spectral contents in the subinertial frequency band and diurnal and its harmonic frequencies (not shown).

Moreover, the spatially averaged energy spectra of detided surface currents are nearly identical (not shown).

2.2 Model configuration

In order to investigate the influence of the coastal boundary on the wind-driven ocean response and to describe the dominant circulation at three different frequencies [low (σ_L), diurnal (σ_D), and inertial (σ_I) frequencies], an ocean model is implemented using the MITgcm (e.g., Marshall et al. 1997), based on the primitive (Navier-Stokes) equations on a sphere under the Boussinesq approximation. The equations are written in z -coordinates and discretized using centered second-order finite difference approximation in a

staggered “Arakawa C-grid.” It has been used in numerous ocean state estimation and adjoint sensitivity studies at global and regional scales (e.g., Stammer et al. 2002; Fukumori et al. 2004; Menemenlis et al. 2005; Hoteit et al. 2009, 2010, 2013; Kohl and Cornuelle 2007; Zhang et al. 2011; Gopalakrishnan et al. 2013a, b). The MITgcm has also been applied in several regional-scale process studies (e.g., Legg et al. 2006; Todd et al. 2011; Edwards et al. 2004a, b) and demonstrated its suitability and adaptability in modeling the regional coastal ocean circulation.

The model domain extends from 32°N to 33°N and from 117°W to 118°W ($\sim 120\text{ km} \times 120\text{ km}$), covering the southern coast of San Diego (Fig. 1). The model bathymetry is extracted from the National Geophysical Data Center

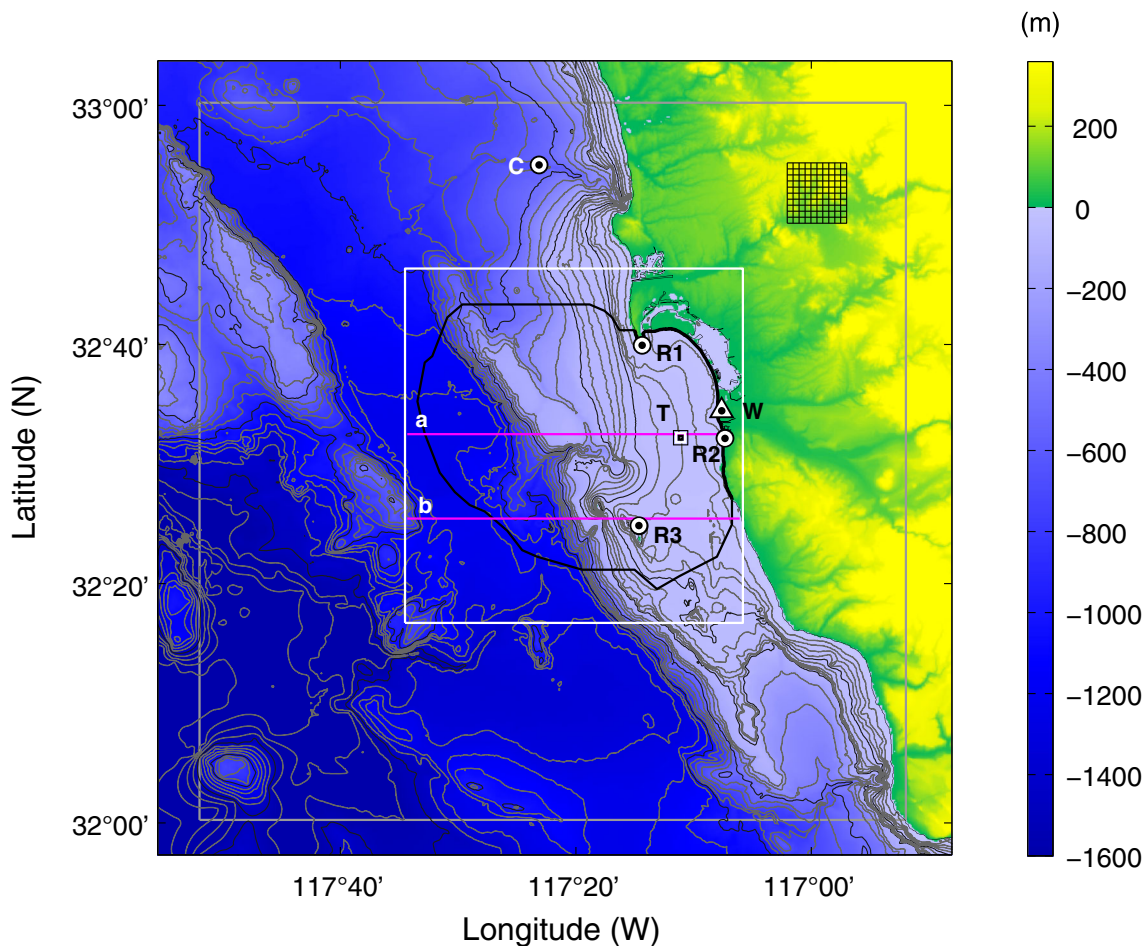


Fig. 1 The study domain for investigation of the influence of coastal boundaries on the local wind-driven circulation and for interpretation of anisotropic wind transfer functions off southern San Diego. The analysis is based on the two-year observations (July 2007 to June 2009) of surface currents from three high-frequency radars [HFR; R1 (Point Loma), R2 (Border Park), and R3 (Coronado Islands)], subsurface currents from ADCP (T), and the wind at the Tijuana River valley (TJR, W). A black outline denotes the effective spatial coverage area of HFRs (at least 70 % data availability for two years). A gray square box indicates the MITgcm domain whose resolution is approximately

1 km ($1^\circ/100$). An example of 10 by 10 model grid points is shown on the top right corner. The initial condition of temperature and salinity of the model is obtained from a CalCOFI station on the Line 93.3 (C). The data- and model-derived transfer functions within a white box are presented for their qualitative comparison. The cross-shore structure of wind transfer functions and momentum terms is considered along cross-shore lines a and b. The bottom bathymetry contours are indicated by thin curves with 10 m ($0 < z < 100\text{ m}$) and 50 m ($100 < z < 1,000\text{ m}$) contour intervals and thick curves at the 50-, 100-, 500-, and 1,000-m depths

(NGDC). The model is integrated on a $1^\circ/100 \times 1^\circ/100$ (1 km horizontal resolution) spherical polar grid, with 40 vertical z -levels. The vertical z -level spacing is 1 m at the surface, and the spacing gradually increases to 1.5 m at 5 m, 2 m at 10 m, 4 m at 20 m, 8 m at 42 m, 20 m at 100 m, 38 m at 200 m, 86 m at 550 m, 132 m at 1,000 m, and 160 m at the maximum bottom depth of 1,800 m. The inner-shelf off southern San Diego (up to 20 m depth) consists of 12 z -levels, which provide the moderate vertical resolution required to simulate the relevant shelf dynamics. In this configuration, the model is operated in a hydrostatic mode with an implicit free surface. The model uses no-slip conditions at the bottom and lateral boundaries and parameterizes bottom friction with a quadratic bottom drag coefficient of 0.001. While the quadratic bottom drag coefficient is dimensionless and the typically suggested value ranges between 0.001 and 0.003, a low value is chosen in this study to prevent the damping of the near-bottom flow energy. The bottom drag represents additional friction (body force), in addition to that imposed by the no-slip condition at the bottom. The drag is cast as a stress, expressed as a quadratic function of the mean flow in the layer above the topography [e.g., Adcroft et al. 2014]. Although the coastal ocean response might be sensitive to the choice of the bottom drag coefficient, the idealized model results presented in this paper are insensitive to the chosen quadratic bottom drag coefficient, and the bottom circulation is less energetic relative to the surface circulation in response to the chosen weak wind stress forcing of 0.01 N m^{-2} . The sub-grid scale physics is approximated by a diffusive operator of second order in the vertical. Vertical diffusivity and viscosity are parameterized by Laplacian mixing with background values of 2×10^{-6} and $2 \times 10^{-4} \text{ m}^2 \text{ s}^{-1}$, respectively, and by the K -profile parameterization (KPP) in the surface mixed layer (Large et al. 1994). In the horizontal grid, diffusive and viscous operators are of second order with coefficients of 5 and $10 \text{ m}^2 \text{ s}^{-1}$, respectively. Since the bottom boundary layer dynamics might influence the oceanic response in the shallow coastal waters, the insufficient representation of the bottom boundary layers in the present model implementation is possibly an important shortcoming of this idealized model study.

Since this model is designed to examine the dynamical components only for the wind-driven coastal circulation, an idealized set of initial and boundary conditions and surface wind forcing are applied. Thus, surface gravity waves, surface heat and salt fluxes, wind stress curl, tidal forcing, and runoff fluxes are not considered in this idealized experiment. The model is initialized using horizontally uniform temperature (T) and salinity (S) data obtained from climatology of California Cooperative Oceanic Fisheries Investigation (CalCOFI) T/S profiles at a station on the Line 93.3 ($32.91^\circ \text{ N } 117.4^\circ \text{ W}$) for 60 years (1950 to 2009),

denoted as C in Fig. 1. The open boundary conditions for this idealized model consists of horizontally uniform T and S profiles with no temporal variability, and the horizontal velocities at the open boundaries are set to zero. In order to examine the influence of seasonal stratification, both summer (June to August) and winter (December to February) T/S profiles are used. Each model simulation is forced uniformly in space with an ideal sinusoidal wind stress with a magnitude of 0.01 N m^{-2} at a given single frequency. Since the idealized model study is purely based on an assumption of a linear response between ocean state and wind forcing, we used a reasonable wind stress forcing, which is comparable to the observed weak wind stress off the San Diego coast (e.g., Kim et al. 2010b), to perturb the ocean so as to simulate a noticeable change in the ocean state. Using adjoint model simulations, this linear relationship has been quantitatively tested by convolving the adjoint sensitivities with the impulse (perturbation) and comparing it with the ocean state differences obtained from the reference (with no perturbation) and the perturbed simulations (e.g., Gopalakrishnan et al. 2013a). However, this adjoint model verification is beyond the scope of this paper.

The wind stress at three different frequencies is applied (e.g., Craig 1989): low ($\sigma = \sigma_L$), diurnal ($\sigma = \sigma_D$), and inertial ($\sigma = \sigma_I$) frequencies. To investigate the anisotropic current responses to the wind, a unidirectional wind stress is applied separately in the x (east-west) and y (north-south) directions. The numerical model is simulated for a period of 30 days, and the model solutions for an initial spin-up time period (three days) are excluded from the estimation of transfer functions. Although the weak near-inertial oscillations still remain in the time series after three days, the model solutions at low frequency reach the equilibrium quickly (Appendix B and Fig. 14).

3 Data analysis

The primary relationship of wind stress with either currents or SSHs is assumed to be linear in this analysis. The Rossby number (R_o), simply defined as the vorticity normalized by local inertial frequency (ζ/f_c), off southern San Diego is in the range of $O(10^{-1})$ to $O(1)$, obtained from statistics of observed surface submesoscale eddies (e.g., Kim 2010). However, the wind-coherent surface currents in this region have the decorrelation length scales of 60 to 80 km (e.g., Kim et al. 2010a), and the relevant Rossby number is expected to be very small ($R_o \ll 1$). Therefore, over most of the domain of interest, the response is nearly linear. Although the nonlinear terms can modify the responses to the onshore and offshore winds (or upcoast and downcoast winds), they are not included in this analysis in order to limit the scope of the paper. An example of nonlinear

data-derived transfer functions was discussed by Kim et al. (2009b).

In order to interpret the statistical analysis (Section 3.1) within the dynamical framework such as momentum balance, we transformed the data-derived transfer functions into the isotropic and anisotropic components (Section 3.2) and connected these components to the terms in the momentum balance (Section 3.3). As both forcing (wind) and response (currents) have directional dependence, i.e., anisotropic response, in the coastal region, we maintain anisotropy in the derivation and transformation in following sections. Since the coastline of the study domain is complicated (e.g., the Point Loma headland), it is difficult to define the along-shore and cross-shore directions. Thus, currents and wind data were not rotated with respect to the orientation of the coastline.

3.1 Wind transfer function

3.1.1 Currents

As the formulation of the anisotropic wind transfer function was addressed by Kim et al. (2009b), the derivations to approximate spatially varying wind stress to spatially uniform wind stress are only presented here. In the frequency domain (σ), the detided currents ($\hat{\mathbf{u}}$) can be decomposed into wind-coherent currents ($\hat{\mathbf{u}}_W$) and residual currents ($\hat{\mathbf{u}}_R$):

$$\hat{\mathbf{u}}(\mathbf{x}, \sigma) = \hat{\mathbf{u}}_W(\mathbf{x}, \sigma) + \hat{\mathbf{u}}_R(\mathbf{x}, \sigma), \quad (1)$$

The wind-coherent currents are defined by the product of the transfer function (\mathcal{G}) and the Fourier coefficients of wind stress ($\hat{\boldsymbol{\tau}}$). The remote wind transfer function may be presented as

$$\hat{\mathbf{u}}_W(\mathbf{x}, \sigma) = \int_{\mathbf{x}'} \mathcal{G}(\mathbf{x}, \mathbf{x}', \sigma) \hat{\boldsymbol{\tau}}(\mathbf{x}', \sigma) d\mathbf{x}'. \quad (2)$$

The wind stress can vary from point to point or be spatially uniform. We assume a spatially uniform wind stress forcing in a region A , leading to the area-averaged impulse response:

$$\hat{\mathbf{u}}_W(\mathbf{x}, \sigma) = \left(\int_{\mathbf{x}' \subset A} \mathcal{G}(\mathbf{x}, \mathbf{x}', \sigma) d\mathbf{x}' \right) \hat{\boldsymbol{\tau}}(\sigma). \quad (3)$$

Thus,

$$\hat{\mathbf{u}}(\mathbf{x}, \sigma) = \mathbf{G}(\mathbf{x}, \sigma) \hat{\boldsymbol{\tau}}(\sigma) + \hat{\mathbf{u}}_R(\mathbf{x}, \sigma), \quad (4)$$

where \mathbf{G} is the transfer function averaged over the area (A). The statistical and theoretical wind transfer functions have been studied extensively (e.g., Ekman 1905; Gonella 1972; Weller 1981; Rio and Hernandez 2003; Elipot and Gille 2009; Kim 2009). The frequency-domain transfer function is computed from the ensemble averaged

covariance of the Fourier coefficients of detided currents and wind stress at each frequency (Eq. 5). The vector quantities of wind stress and currents can be considered as (1) a scalar combined with a complex notation for the isotropic analysis (Appendix C) or (2) individual vector components for the anisotropic analysis. While the isotropic transfer function can be useful and convenient to present the statistical relationship between wind stress and currents (e.g., Kim et al. 2009b), the anisotropic transfer function can separate the phase and veering angle (see Appendix D for more details). For anisotropic estimates, these vector components are considered separately in the x and y directions, so the estimated transfer function matrix is as follows:

$$\mathbf{G}(\mathbf{x}, \sigma) = \left(\langle \hat{\mathbf{u}}(\mathbf{x}, \sigma) \hat{\boldsymbol{\tau}}^\dagger(\sigma) \rangle \right) \left(\langle \hat{\boldsymbol{\tau}}(\sigma) \hat{\boldsymbol{\tau}}^\dagger(\sigma) \rangle + \mathbf{R} \right)^{-1}, \quad (5)$$

where \mathbf{R} denotes a regularization matrix, \dagger is the complex conjugate transpose, and $\langle \cdot \rangle$ indicates the ensemble average (see Kim et al. 2009b, 2010b for more details). In the following, u and v denote the current components in the x and y directions, respectively.

Expanding into components to allow for anisotropy, the observed wind-coherent currents [$\hat{\mathbf{u}}_W = (\hat{u}_W, \hat{v}_W)$] are presented as

$$\hat{u}_W(\mathbf{x}, \sigma) = \mathbf{G}_{xx}(\mathbf{x}, \sigma) \hat{\boldsymbol{\tau}}_x(\sigma) + \mathbf{G}_{xy}(\mathbf{x}, \sigma) \hat{\boldsymbol{\tau}}_y(\sigma), \quad (6)$$

$$\hat{v}_W(\mathbf{x}, \sigma) = \mathbf{G}_{yx}(\mathbf{x}, \sigma) \hat{\boldsymbol{\tau}}_x(\sigma) + \mathbf{G}_{yy}(\mathbf{x}, \sigma) \hat{\boldsymbol{\tau}}_y(\sigma), \quad (7)$$

where the first and second subscripts of transfer functions ($\mathbf{G}_{\{\cdot\}\{\cdot\}}$) denote the direction of the current and wind stress, respectively. The corresponding magnitude and argument are referred to as $G_{\{\cdot\}\{\cdot\}}$ and $\Theta_{\{\cdot\}\{\cdot\}}^G$, i.e.,

$$\mathbf{G}_{\{\cdot\}\{\cdot\}} = G_{\{\cdot\}\{\cdot\}} \exp\left(i\Theta_{\{\cdot\}\{\cdot\}}^G\right). \quad (8)$$

The argument of the isotropic transfer function indicates both the phase difference in the frequency domain (or time lag in the time domain) and the veering angle between wind stress and currents (e.g., Kim et al. 2010b). In contrast, the argument of the anisotropic transfer function implies only the phase difference (or time lag). Thus, the negative argument indicates that wind stress leads currents, and the positive argument means that wind stress follows currents. When $\Theta = \pm 180^\circ$, wind stress and currents appear its maximum and minimum in the opposite timing, respectively (see Appendix D for more details).

3.1.2 Sea surface heights

In a similar way, the observed wind-coherent SSHs ($\hat{\eta}_W$) are expressed by the transfer function of SSHs (\mathbf{g}) and the Fourier coefficients of wind stress:

$$\hat{\eta}_W(\sigma) = \mathbf{g}_x(\sigma) \hat{\boldsymbol{\tau}}_x(\sigma) + \mathbf{g}_y(\sigma) \hat{\boldsymbol{\tau}}_y(\sigma), \quad (9)$$

and the magnitude and argument of transfer functions are given by $g_{\{\cdot\}}$ and $\theta_{\{\cdot\}}^g$, respectively. As the model does not include tidal forcing, η refers to SSH anomalies (SSHAs) with barotropic tide-coherent variance removed.

For convenience in describing the comparison between simulations and observations, the magnitude and argument of model-derived transfer functions for currents and SSHs are denoted differently as $H_{\{\cdot\}\{\cdot\}}$ and $\Theta_{\{\cdot\}\{\cdot\}}^H$, respectively, and $h_{\{\cdot\}}$ and $\theta_{\{\cdot\}}^h$.

The data-derived transfer functions are computed from the covariance of the Fourier coefficients averaged over N ensemble members, created by partitioning the 731-day long hourly time series into N nonoverlapping chunks. N is chosen as 56 to separate the diurnal ($\sigma = \sigma_D$) and inertial ($\sigma = \sigma_f$) frequencies. The difference of these two frequencies sets the maximum bin size in the finite frequency axis ($\Delta\sigma = 0.0767$ cpd = $1/731$ cpd \times 56). The estimate of the transfer function at each frequency is based on $2N$ degrees of freedom based on the chi-squared distribution (e.g., Chapter 9 in Young (1999), Chapter 12.5 in von Storch and Zwiers (1999)). However, considering the overlapped spectral contents at low frequency, the degrees of freedom can be lower than $2N$. Moreover, the nonzero lowest frequency ($\sigma = 0.0767$ cpd) is equal to the low frequency (σ_L) in this paper.

3.2 Transformation to isotropic and anisotropic components

The anisotropic transfer functions can be separated into purely isotropic components (ISCs; $I_{\{\cdot\}}$) and anisotropic components (ASCs; $A_{\{\cdot\}}$):

$$I_d = \frac{G_{xx} + G_{yy}}{2}, \tag{10}$$

$$I_c = \frac{G_{xy} - G_{yx}}{2}, \tag{11}$$

$$A_d = \frac{G_{xx} - G_{yy}}{2}, \tag{12}$$

$$A_c = \frac{G_{xy} + G_{yx}}{2}, \tag{13}$$

where the subscripts d and c indicate the diagonal terms (the wind and current responses are parallel to each other) and cross terms (the wind and current responses are normal to each other), respectively. Their magnitude and argument are $I_{\{\cdot\}}$ and $\Theta_{\{\cdot\}}^I$, respectively, and $A_{\{\cdot\}}$ and $\Theta_{\{\cdot\}}^A$.

The wind-coherent currents (Eqs. 6 and 7) can be presented in terms of ISCs and ASCs:

$$\hat{u}_W(\sigma) = [I_d(\sigma) + A_d(\sigma)] \hat{\tau}_x(\sigma) + [I_c(\sigma) + A_c(\sigma)] \hat{\tau}_y(\sigma), \tag{14}$$

$$\hat{v}_W(\sigma) = [-I_c(\sigma) + A_c(\sigma)] \hat{\tau}_x(\sigma) + [I_d(\sigma) - A_d(\sigma)] \hat{\tau}_y(\sigma). \tag{15}$$

The ISCs and ASCs can be used to constrain the expected amount of anisotropy in the prior statistics for the estimate

of the data-derived transfer function (see Appendix E for more details). The ISCs and ASCs are computed using predetermined priors, then are transformed into transfer functions (Eqs. 14 and 15). The data-derived ISCs and ASCs (I_d , I_c , A_d , and A_c) can be found by solving coupled Eqs. 14 and 15 frequency by frequency (see Appendix E). Similar to the transfer functions, the model-derived ISCs and ASCs are referred to as $J_{\{\cdot\}}$ and $B_{\{\cdot\}}$. In some cases the current response to wind stress is not well-determined due to low signal-to-noise ratio (SNR) in the observations, and estimating ISCs and ASCs separately can prevent artificial anisotropy.

3.3 Momentum balance

The model provides time series of individual terms in the momentum equations (e.g., Gill 1982) which take the form of

$$\underbrace{\frac{\partial \mathbf{u}}{\partial t}}_{TD} + \underbrace{\mathbf{u} \cdot \nabla \mathbf{u}}_{AD} + \underbrace{f_c \times \mathbf{u}}_{CR} = \underbrace{-\frac{1}{\rho} \nabla p}_{PG} + \underbrace{\nabla_h (A_h \nabla_h \mathbf{u})}_{HD} + \underbrace{\frac{\partial}{\partial z} \left(A_z \frac{\partial \mathbf{u}}{\partial z} \right)}_{VD}, \tag{16}$$

where ρ , f_c , A_h , and A_z denote the density, Coriolis frequency, and scalar horizontal viscosity, and vertical eddy viscosity, respectively (∇_h is the horizontal derivative). The individual terms, i.e., TD, AD, CR, PG, HD, and VD indicate tendency, advection, Coriolis, pressure gradients, and horizontal and vertical dissipation (viscous forcing), respectively. The surface wind stress is applied to the model as the surface boundary condition of the VD term. In order to allow anisotropic response, the momentum equations in the x and y directions are considered separately instead of being combined using a complex notation. In the model experiments, a unidirectional wind stress (τ_x or τ_y) is applied, so the individual terms in Eq. 16 can be collected into four groups similar to the anisotropic transfer functions (Eqs. 6 and 7).

The components of transfer functions and the momentum equations describe the same coastal ocean system; however, they are not always corresponding one to another. Thus, the anisotropic transfer functions sometimes can be described with a combination of terms in the momentum equations, which can make the interpretation of their physical meaning complicated.

4 Results

The wind transfer functions derived from observations and model simulations are examined at three frequencies, i.e., low ($\sigma_L = 0.0767$ cpd), diurnal ($\sigma_D = 1$ cpd), and inertial ($\sigma_f = 1.07$ cpd) frequencies. The time-dependent model state forced by spatially uniform wind stress at a specific

frequency is fit by sine and cosine functions at the forcing frequency at each grid point, excluding a spin-up time of three days (Appendix B and Fig. 14). The magnitudes of the computed Fourier coefficients are presented as a horizontal map ($x - y$ section) and as a subsurface transect along a cross-shore line ($x - z$ section; line a or b) in Fig. 1. The model results are shown only for the subdomain (white box in Fig. 1) to match the HFR coverage (a black curve in Fig. 1) in order to ease qualitative comparison. The magnitudes of data-derived and model-derived transfer functions have qualitative similarity in their spatial structure, but the observed responses and spatial scales are larger than the modeled ones (see Section 5.4 for more discussion).

As the local inertial frequency ($\sigma_f = 1.07$ cpd) in the study area and the diurnal frequency ($\sigma_D = 1$ cpd) are close, the circulation at those frequencies can be lumped into near-inertial circulation. However, as the observed currents are weak at the inertial frequency and strong at the diurnal frequency and this work may also be applicable to other coastal regions where there is significant separation of variance between the two frequencies, we present them separately.

4.1 Subinertial circulation

The wind-driven subinertial circulation in the coastal region is characterized by the Ekman balance in the surface Ekman layer and the geostrophic balance near the coastal boundary and below the Ekman layer. Not only geostrophic balance but frictional balance due to coastal boundary (e.g., shoreline and bottom topography) appears in the data-derived transfer functions to some degree.

4.1.1 Transfer functions

Surface At low frequency, the observed and modeled wind transfer functions (G_{yy} and H_{yy}) are both enhanced near the coast, i.e., in the area within 25 km (G_{yy}) and 8 km (H_{yy}) from the coast (Fig. 2d and l) of which spatial mismatch is discussed in Section 5.4. Although G_{xx} and G_{xy} contain spatial structures due to the HFR beam pattern, G_{xx} shows regions of the enhanced response, similar to H_{xx} (e.g., off the southern tip of Point Loma and San Diego Bay mouth in Fig. 2a and i). Furthermore, G_{yx} and H_{yx} have moderately enhanced magnitudes near the coast where the current is normal to the wind direction (Fig. 2c and k). Relatively weaker spatial structures of G_{xy} and H_{xy} appear in just south of Point Loma and near the Coronado Islands (Fig. 2b and j). The arguments of the model-derived and data-derived transfer functions are consistent within $\pm 20^\circ$ (Θ^G in Fig. 2e–h and Θ^H in Fig. 2m–p). The cross-shore wind stress and the along-shore currents have the nearly 180° argument

difference, which means that their maximum and minimum have the opposite timings (see Section 5.1).

The enhanced modeled SSH responses (h_x and h_y) extend 10 to 16 km from the coast (Fig. 2q and r), and they are also visible near the closed model boundaries (not shown). This marks the regions where the PG term may be important; however, it does not appear in the analysis of the momentum terms (see Section 4.2.2). Both θ_x^h and θ_y^h rotate clockwise near the coast and their nodal points are located to the west of Point Loma (Fig. 2s) and far offshore (outside of the figure; Fig. 2t), respectively. Four terms of the wind-current transfer function are translated into two terms of the wind-SSHs transfer function. In other words, h_x contains characteristics of H_{xx} and H_{yx} (Fig. 2q, i, and k), and h_y contains primary features in H_{xy} and H_{yy} (Fig. 2r, j and l).

Subsurface The data-derived subsurface transfer functions at location T (Fig. 1) are presented for all frequencies in Fig. 3, overlaid with transfer functions of HFR surface currents at that location. Although they are independent observations, the magnitudes and arguments of transfer functions at the surface and subsurface are nearly consistent except for an abrupt decrease in downwind magnitudes (G_{xx} and G_{yy} in Fig. 3a and d) between the surface and the top bin (4.3 m) of the ADCP. An analytical Ekman model can provide an intuitive way to interpret the data-derived transfer function (Appendix C). The observed mixed layer is estimated to be approximately 6 to 8 m, where the magnitudes and arguments above and below the inertial frequency change with the analytical model coherently (Fig. 15).

At low frequency ($\sigma = \sigma_L$), enhanced G_{xx} , G_{yx} , and G_{yy} appear throughout the water column, and the vertical structure of their arguments becomes smooth (Fig. 3a–h). On the contrary, in the subinertial frequency band ($\sigma_L < \sigma < \sigma_f$), G_{xx} and G_{yy} sharply decrease from surface to subsurface, but are somewhat enhanced in the middle of the water column (10 to 22 m depth) (Fig. 3a and d).

In the numerical model, the magnitudes of low-frequency transfer functions (H) are intensified near the surface, and a rapid shift of their arguments (Θ^H) appears at the bottom of the mixed layer approximately 8 m depth (Fig. 4). The enhanced features in H_{yy} are more concentrated at the surface than the subsurface within 5 km from the coast (Fig. 4d). The geostrophic currents near the bottom shelf are manifested in H_{yx} and H_{yy} (Fig. 4c and d). H_{xx} and H_{xy} along this x -directional line do not show the enhanced surface current response near the coast (Fig. 4a and b).

The negative Θ_{yy}^H within 10 km from the coast appears when the geostrophic balance overrides the frictional balance (Fig. 4h). Θ_{yy}^H shows the balanced flux across the transect between enhanced near-coast currents (negative arguments) and the weak currents in the nearly opposite

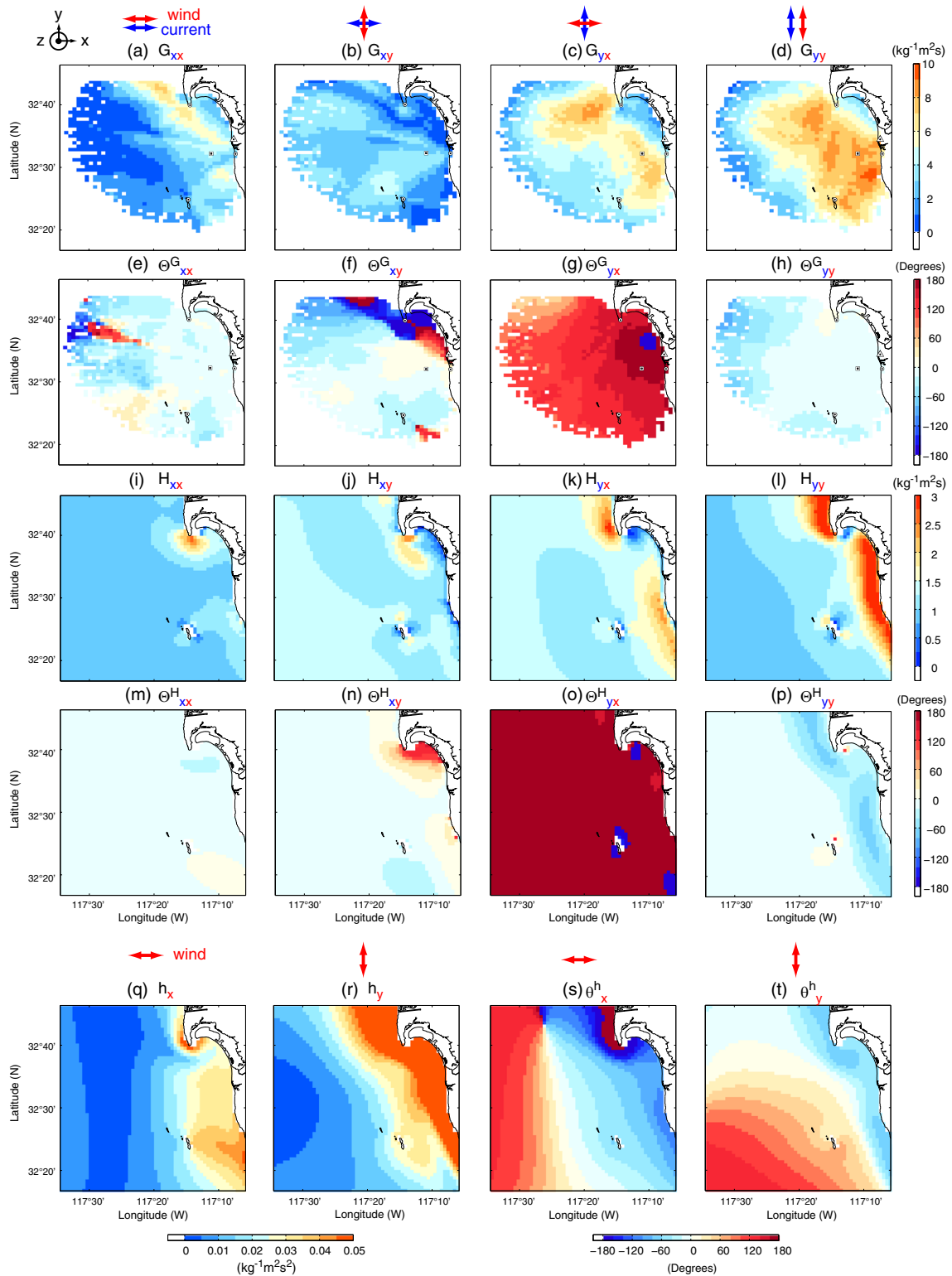


Fig. 2 Magnitudes and arguments of anisotropic wind transfer functions of surface currents and SSHs at low frequency ($\sigma = \sigma_L$). **a–h**, **i–p**, and **q–t** denote the data-derived and model-derived transfer functions for surface currents, and model-derived transfer functions for SSHs, respectively. **a** G_{xx} , **b** G_{xy} , **c** G_{yx} , **d** G_{yy} , **e** Θ_{xx}^G , **f** Θ_{xy}^G , **g** Θ_{yx}^G ,

h Θ_{yy}^G , **i** H_{xx} , **j** H_{xy} , **k** H_{yx} , **l** H_{yy} , **m** Θ_{xx}^H , **n** Θ_{xy}^H , **o** Θ_{yx}^H , **p** Θ_{yy}^H , **q** h_x , **r** h_y , **s** θ_x^h , and **t** θ_y^h . The directions of wind stress and currents are marked on the top of each column. **a–p** and **q–t** share a colorbar on the right of each row and the colorbar on the bottom, respectively. See Section 3 for convention of subscripts and superscripts

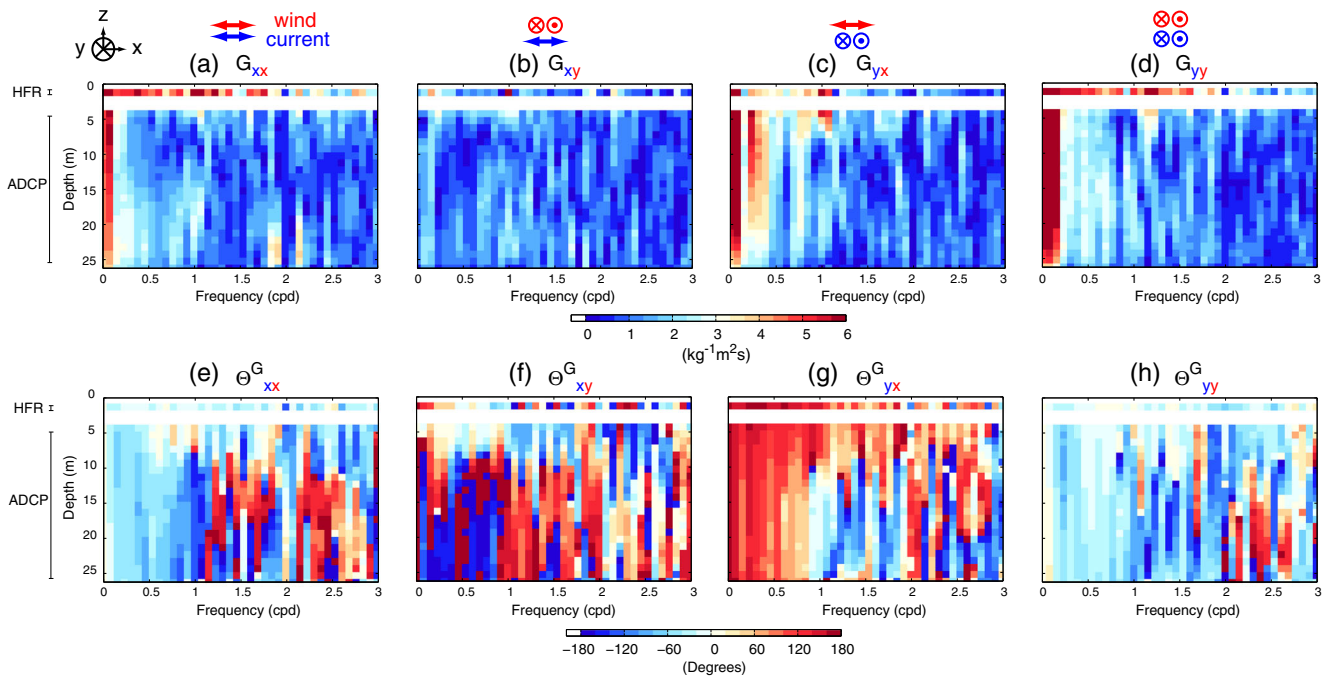


Fig. 3 Magnitudes and arguments of surface and subsurface data-derived anisotropic wind transfer functions derived from HFRs and ADCP observations at T in Fig. 1. **a** G_{xx} , **b** G_{xy} , **c** G_{yx} , **d** G_{yy} , **e** Θ_{xx}^G , **f** Θ_{xy}^G , **g** Θ_{yx}^G , and **h** Θ_{yy}^G . The directions of wind stress and currents are

marked on the top of each column. **a–d** and **e–h** share a colorbar on the bottom, respectively. See Section 3 for convention of subscripts and superscripts

direction (positive arguments). Below the mixed layer, the arguments vary continuously in the x and z directions.

4.1.2 Momentum balance

Like the model state, the terms in the model momentum equations were projected on the forcing frequency by a least-squares fit. Referring to Eq. 16, horizontal dissipation (HD), advection (AD), and tendency (TD) were all negligible as the sum of these three terms is less than 3 % of the total variance everywhere. The dominant terms are Coriolis (CR), vertical dissipation (VD), and pressure gradients (PG). The terms in the momentum equations balance in both time and frequency domains. However, the magnitudes in the frequency domain, i.e., the absolute values of Fourier coefficients, may not be balanced, particularly, in the figure presentations. For instance, when a complex number is equal to the sum of two different complex numbers ($a = b + c$), their absolute values may not be always equivalent ($|a| \leq |b| + |c|$).

Near the coast Within about 8 km from shore, PG becomes important, balancing CR in some regions near the shore (Figs. 5 and 6):

$$-f_c v = -g \frac{\partial \eta}{\partial x} + \frac{\partial}{\partial z} \left(A_z \frac{\partial u}{\partial z} \right), \quad (17)$$

$$f_c u = -g \frac{\partial \eta}{\partial y} + \frac{\partial}{\partial z} \left(A_z \frac{\partial v}{\partial z} \right). \quad (18)$$

The difference of magnitude of low-frequency $\partial \eta / \partial x$ and $\partial \eta / \partial y$ produces anisotropic wind-forced circulation in the coastal region (middle column in Fig. 5). The enhanced magnitudes near the coast are attributed to pressure gradients against the coast (middle column in Fig. 5) balanced against the Coriolis force (left column in Fig. 5). The PG response to y -directional wind stress is much larger than the one to x -directional wind stress and is dominated in the direction normal to the applied wind stress. For x -directional wind stress (roughly cross-shore at the line, corresponding to Fig. 6), a small amount of PG and CR (geostrophic balance) is seen, intensified near the shore, and it dominates below the frictional surface layer in Fig. 6. For y -directional wind stress (roughly along-shore at this line), the geostrophic balance is dominant near the shore, supporting the hypothesis that the presence of the coastal boundaries allows the pressure gradients to balance the Coriolis force on the along-shore flow and enhances the response to the wind.

In the surface layer at low frequency, surface zonal currents due to τ_y converge or diverge at the coastal boundaries producing x -directional pressure gradients ($\partial \eta / \partial x$) and then geostrophic currents. Thus, G_{yy} and H_{yy} are enhanced near the coast parallel to the wind direction (Figs. 2d, 1 and 4d). In a similar way, the zonal geostrophic

currents driven by the y -directional pressure gradients ($\partial\eta/\partial y$) due to τ_x cause the increased magnitudes at the boundaries parallel to the wind direction (e.g., the southern tip of Point Loma and San Diego Bay mouth) (H_{xx} in Fig. 2i).

In contrast, the y -directional pressure gradients ($\partial\eta/\partial y$) due to τ_y at the coast cause zonal geostrophic currents, which contribute to the magnitudes of G_{xy} and H_{xy} (Fig. 2b and j). Likewise, G_{yx} and H_{yx} include meridional geostrophic currents due to τ_x (Figs. 2c, k and 4c).

Offshore In the surface layer (magnitudes shown in Fig. 5), the CR and VD terms were the dominant balance offshore, where the PG term was negligible, as expected:

$$f_c \times \mathbf{u} = \frac{\partial}{\partial z} \left(A_z \frac{\partial \mathbf{u}}{\partial z} \right). \tag{19}$$

A vertical section in the cross-shore direction (line a in Fig. 1) shows that, for both wind directions, the balance of CR and VD is restricted to an approximately 10-m surface layer resembling a slab layer (Figs. 5 and 6). Some rotation in the balance can be seen within the layer, but it resembles a slab layer more than a classic Ekman layer because of non-constant vertical eddy viscosity in the surface boundary layer. The frictional term (VD) in the direction where wind stress is applied has 30 to 40 % higher magnitudes than those in the other direction (Fig. 6c and l vs. f and i). In other words, the frictional forces normal to wind stress are less than the ones parallel to wind stress.

Near the bottom The geostrophic balance appears near a 10 m depth which transits from the frictional balance in the surface mixed layer (Fig. 6):

$$f_c \times \mathbf{u} = -\frac{1}{\rho} \nabla p. \tag{20}$$

The flows near the bottom reflect the changes around 20-m isobath. The vertical grid spacing in the model does not vary drastically over the shelf-slope region (4 m grid spacing at 20 m depth with 12 z -levels, and 8 m grid spacing at 40 m depth with 16 z -levels) and provides the moderate resolution to simulate the realistic near-bottom circulation. The energy due to the near-bottom flow is very low in this idealized simulation forced with a weak wind stress of 0.01 N m^{-2} . Although the model results were not tested by varying the vertical grid resolution offshore of the 20-m isobath, it is unlikely that the near-bottom grid resolution affects the energetic near-bottom shelf circulation of this idealized simulation.

4.2 Circulation at diurnal and inertial frequencies

The near-inertial internal oscillations in this analysis are locally driven by spatially uniform and periodic wind stress, which creates a shelf circulation that interacts with the coastal boundaries. This differs from studies with wind fields having rapid spatial and temporal changes, i.e., translating wind storms (e.g., Pollard and Millard 1970; D’Asaro 1985; Crawford and Large 1996; Davies and Xing 2003). The presence of the coastal boundary generates not only surface pressure gradients due to the no-normal

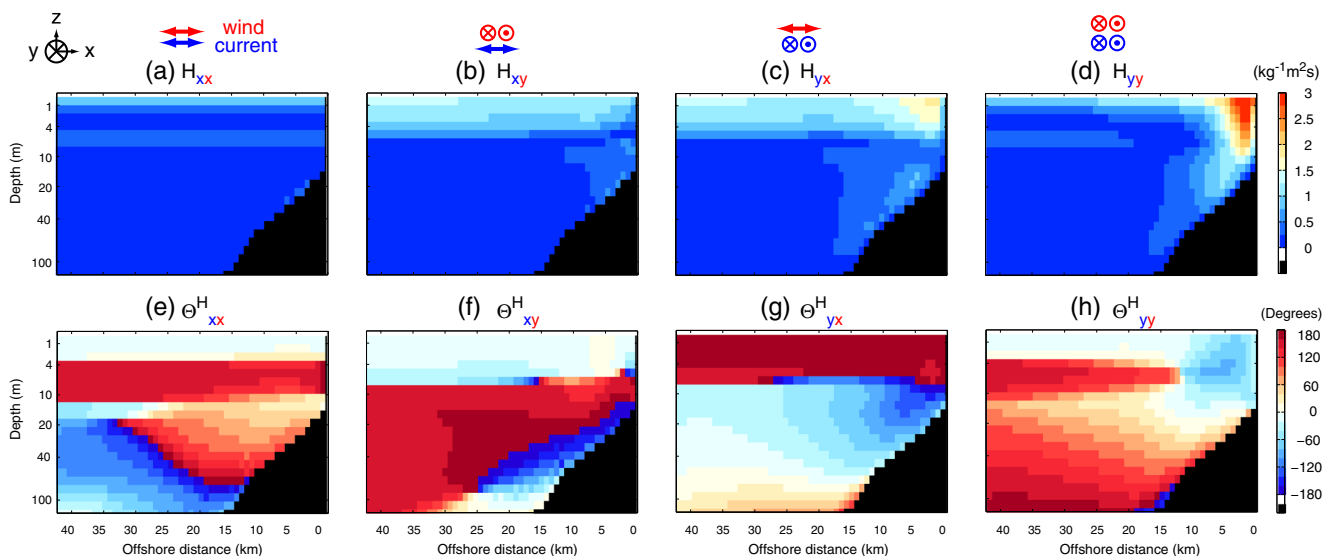


Fig. 4 Magnitudes and arguments of model-derived anisotropic wind transfer functions at low frequency ($\sigma = \sigma_L$) along a cross-shore line a in Fig. 1. **a** H_{xx} , **b** H_{xy} , **c** H_{yx} , **d** H_{yy} , **e** Θ_{xx}^H , **f** Θ_{xy}^H , **g** Θ_{yx}^H , and **h** Θ_{yy}^H . The directions of wind stress and currents are marked

on the top of each column. **a–h** share a colorbar on the right. See Section 3 for convention of subscripts and superscripts. Note that the depth is nonlinearly scaled to highlight the near-surface feature

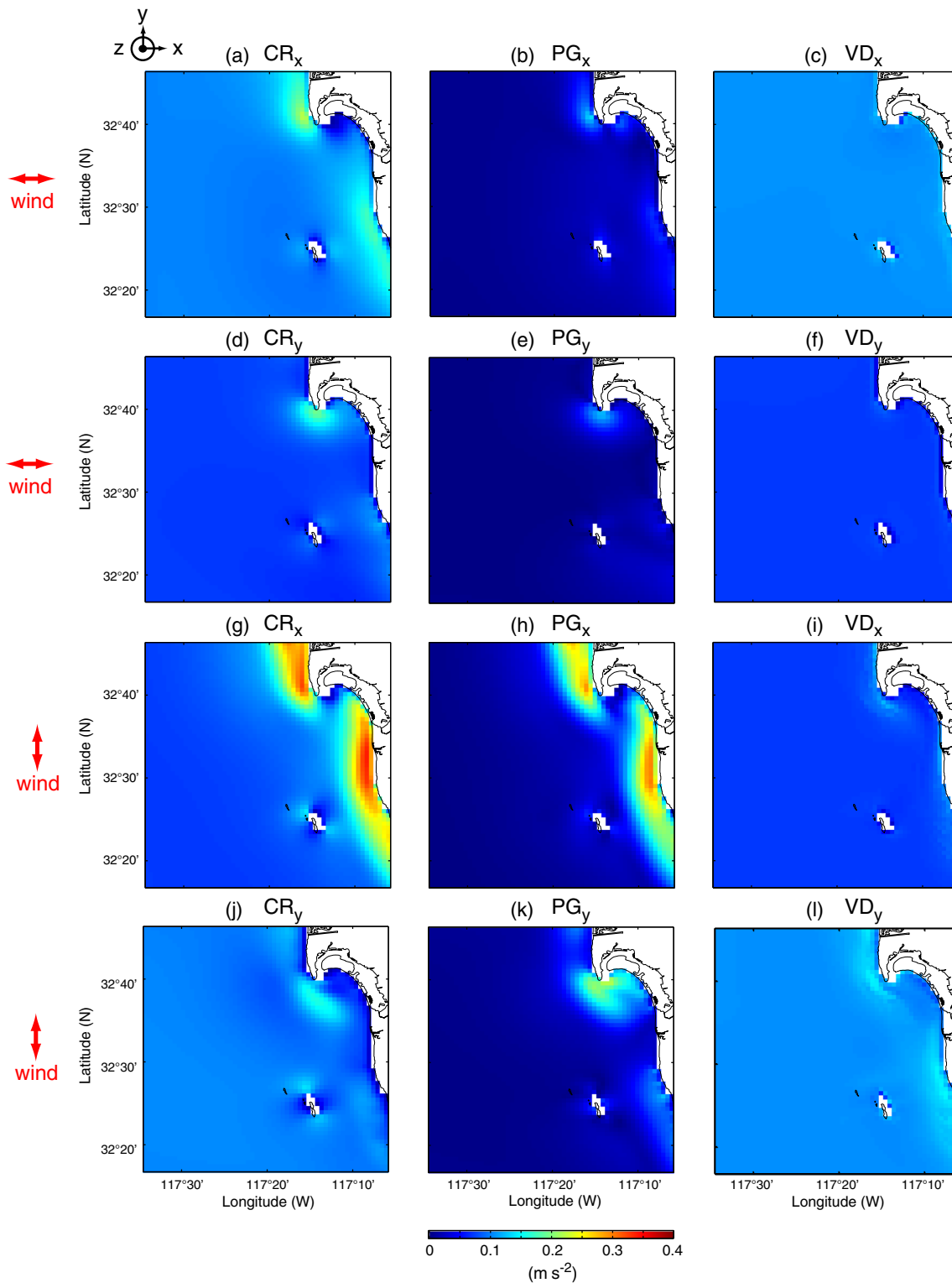


Fig. 5 Magnitudes of Fourier coefficients of CR, PG, and VD terms ($\times 10^5, \text{m s}^{-2}$) at low frequency ($\sigma = \sigma_L$) and the top vertical layer ($z = z_0$). **a–c** x -directional momentum terms to τ_x . **a** CR_x ($-f_c v$), **b** PG_x ($-g \partial \eta / \partial x$), and **c** VD_x ($A_z \partial^2 u / \partial z^2$). **d–f** y -directional momentum terms to τ_x . **d** CR_y ($f_c u$), **e** PG_y ($-g \partial \eta / \partial y$), and **f** VD_y ($A_z \partial^2 v / \partial z^2$). **g–i** x -directional

momentum terms to τ_y . **g** CR_x ($-f_c v$), **h** PG_x ($-g \partial \eta / \partial x$), and **i** VD_x ($A_z \partial^2 u / \partial z^2$). **j–l** y -directional momentum terms to τ_y . **j** CR_y ($f_c u$), **k** PG_y ($-g \partial \eta / \partial y$), and **l** VD_y ($A_z \partial^2 v / \partial z^2$). The directions of wind stress are marked on the left of each row. **a–l** share a color bar on the bottom. See Section 3 for convention of subscripts and superscripts

flow condition but also internal pressure gradients along with internal waves propagating offshore when stratification is present (e.g., Xing and Davies 2004; Davies 2003). The vertical structure of near-inertial currents in the upper

ocean is expected to be dominated by the first baroclinic mode with a 180° argument difference between below and above the thermocline (e.g., Millot and Crepon 1981; Chen et al. 1996).

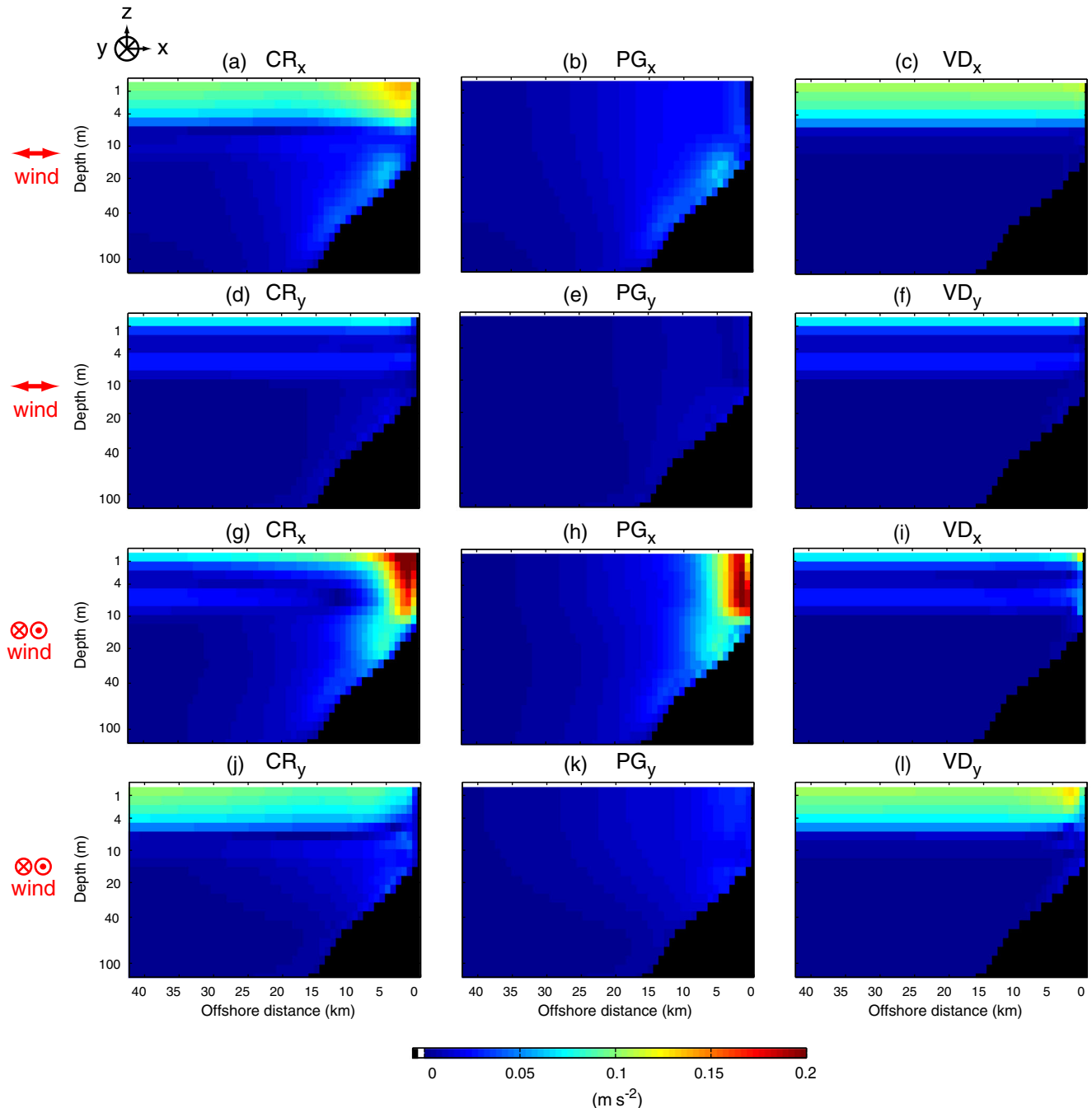


Fig. 6 Magnitudes of Fourier coefficients of CR, PG, and VD terms ($\times 10^5$, m s^{-2}) at low frequency ($\sigma = \sigma_L$) and along a cross-shore line **a** in Fig. 1. **a–c**: x -directional momentum terms to τ_x . **a** CR_x ($-f_c v$), **b** PG_x ($-g \partial \eta / \partial x$), and **c** VD_x ($A_z \partial^2 u / \partial z^2$). **d–f**: y -directional momentum terms to τ_x . **d** CR_y ($f_c u$), **e** PG_y ($-g \partial \eta / \partial y$), and **f** VD_y ($A_z \partial^2 v / \partial z^2$). **g–i**: x -directional momentum terms to τ_y .

g CR_x ($-f_c v$), **h** PG_x ($-g \partial \eta / \partial x$), and **i** VD_x ($A_z \partial^2 u / \partial z^2$). **j–l**: x -directional momentum terms to τ_y . **j** CR_y ($f_c u$), **k** PG_y ($-g \partial \eta / \partial y$), and **l** VD_y ($A_z \partial^2 v / \partial z^2$). The directions of wind stress are marked on the left of each row. **a–l** share a colorbar on the bottom. See Section 3 for convention of subscripts and superscripts. Note that the depth is nonlinearly scaled to highlight the feature in the surface layer

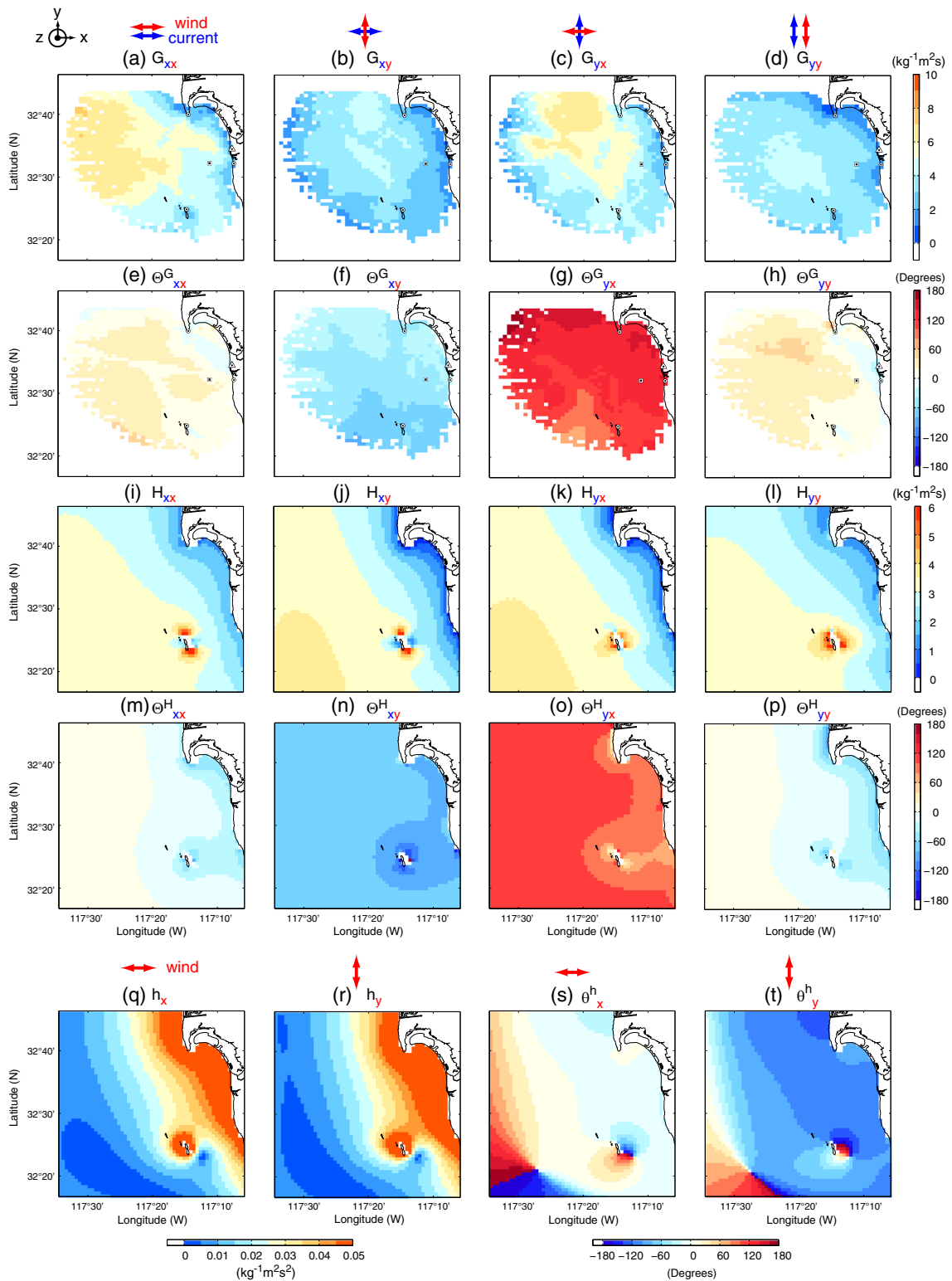


Fig. 7 Magnitudes and arguments of anisotropic transfer functions of surface currents and SSHs at the diurnal frequency ($\sigma = \sigma_D$). **a–h**, **i–p**, and **q–t** denote the data-derived and model-derived transfer functions for surface currents, and model-derived transfer functions for SSHs, respectively. **a** G_{xx} , **b** G_{xy} , **c** G_{yx} , **d** G_{yy} , **e** Θ_{xx}^G , **f** Θ_{xy}^G , **g** Θ_{yx}^G , **h** Θ_{yy}^G , **i** H_{xx} ,

j H_{xy} , **k** H_{yx} , **l** H_{yy} , **m** Θ_{xx}^H , **n** Θ_{xy}^H , **o** Θ_{yx}^H , **p** Θ_{yy}^H , **q** h_x , **r** h_y , **s** θ_x^h , and **t** θ_y^h . The directions of wind stress and currents are marked on the top of each column. **a–p** and **q–t** share a colorbar on the right of each row and the colorbars on the bottom, respectively. See Section 3 for convention of subscripts and superscripts

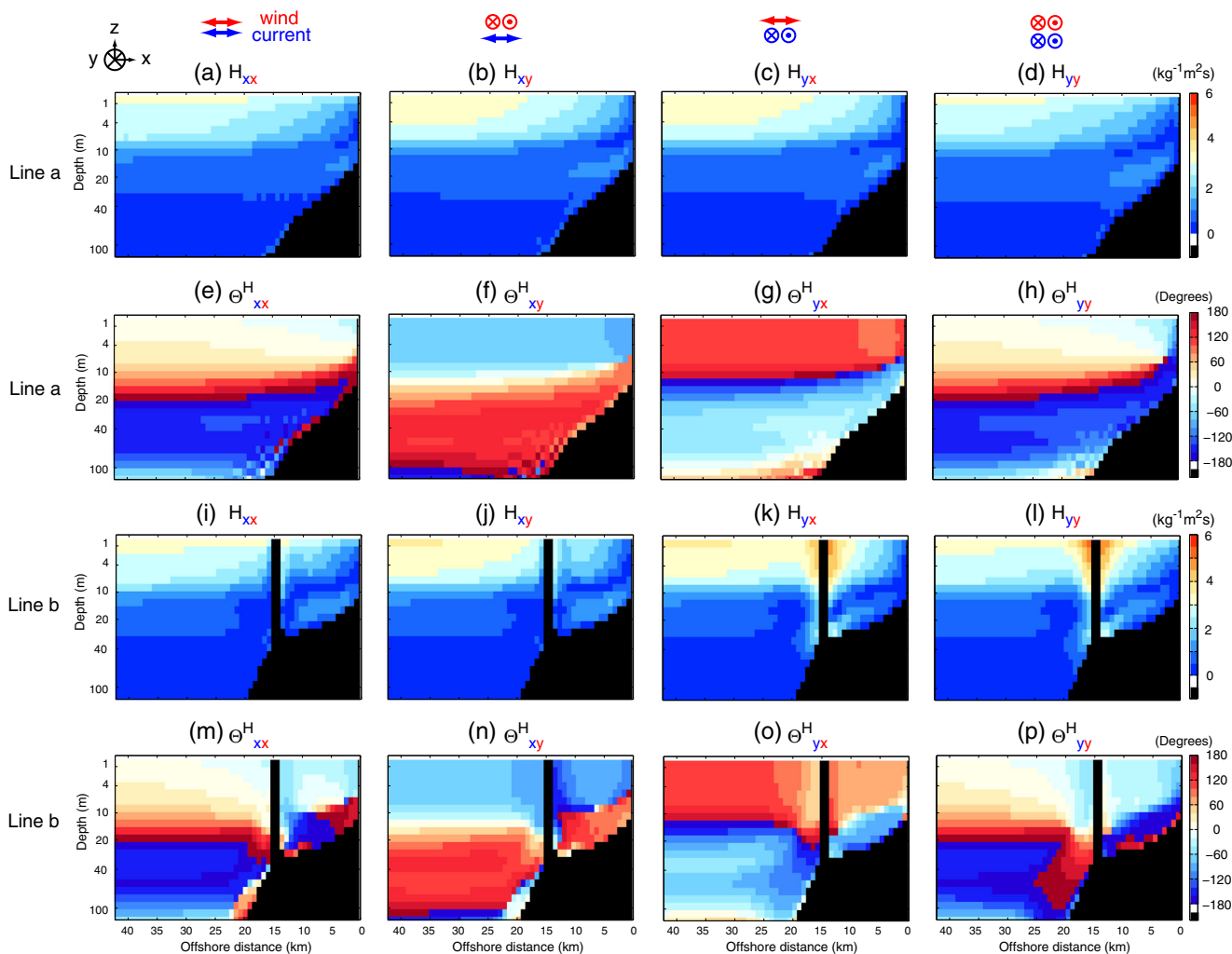


Fig. 8 Magnitudes and arguments of transfer functions of subsurface currents at the diurnal frequency ($\sigma = \sigma_D$) along two cross-shore lines [a–h for the line a and i–p for a cross-shore line b in Fig. 1]. a and i H_{xx} , b and j H_{xy} , c and k H_{yx} , d and l H_{yy} , e and m Θ_{xx}^H , f and n Θ_{xy}^H ,

g and o Θ_{yx}^H , h and p Θ_{yy}^H . The directions of wind stress and currents are marked on the top of each column. a–p share a colorbar on the right. See Section 3 for convention of subscripts and superscripts. Note that the depth is nonlinearly scaled to highlight the near-surface feature

The long-term in situ observations of surface and subsurface currents off southern San Diego exhibit neither any significant variance at the inertial frequency nor a cusped peak in the near-inertial frequency band (see Section 5.3 for more details). The SNR of wind stress at the diurnal frequency is much higher than that at the inertial frequency, which gives better estimates of the wind transfer function at the diurnal frequency (Kim et al. 2010b). The transfer functions and momentum balances at these two nearby frequencies ($\sigma_f - \sigma_D = 0.07$ cpd) have similar spatial structure except for the differences in magnitudes and near-inertial internal oscillations (e.g., Millero and Poison 1981; Davies 2003). Thus, we present the results at the diurnal frequency to compare the statistical and dynamical analyses (Sections 4.2.1 and 4.2.2) and the outcomes at the inertial frequency to describe the internal wave features associated

with seasonal stratification (Section 4.2.3). In order to show the influence of islands, we examine the subsurface transfer functions and momentum balance along two cross-shore sections (lines a and b in Fig. 1). Analysis of observed surface currents having significant variance in the near-inertial frequency band, unambiguous with the diurnal winds and tides, can be found elsewhere (e.g., Shay et al. 1998).

4.2.1 Transfer functions

All four components of model-derived transfer functions (H) at the diurnal frequency appear the reduced magnitudes near the coast and enhanced responses offshore (Fig. 7i and l). Moreover, the enhanced responses appear around islands parallel to the direction of currents. Considering their arguments of transfer functions, all components can be paired

($H_{xx} = H_{yy}$ and $H_{xy} = -H_{yx}$; Figs. 7i–p) except for near-coast regions. In the data-derived transfer function (G), only G_{xx} has spatial structure that matches the model-derived transfer function (H_{xx}), whereas the magnitudes of the other components (G_{xy} , G_{yx} , and G_{yy}) decrease at the periphery of the HFR footprint (Fig. 7a–d). The arguments of both transfer functions (Θ^G and Θ^H) have almost spatially uniform values (Fig. 7e–h and m–p).

The magnitudes of the model-derived SSH responses have a similar spatial pattern for both h_x and h_y with increased magnitudes near the coast and around the islands (Fig. 7q and r). The nodal points of arguments of both model-derived SSH responses (θ_x^h and θ_y^h) are located at the same place (Fig. 7s and t).

In the vertical transects of the transfer function, the magnitudes are intensified in the upper 10 m (first and third rows of Fig. 8). The features of near-inertial internal waves are weakly visible at about 40 m depth and become discernible on the west side of the islands (Fig. 8a–d and i–l). Those features are also evident in the momentum balance at the inertial frequency (not shown).

4.2.2 Momentum balance

At low frequency, the geostrophic currents normal to the pressure gradients are the primary contributor in the

nearshore momentum balance, whereas at the diurnal and inertial timescales, both current components (u and v) normal and parallel to the pressure gradients should be included in the momentum balance (Eqs. 22 and 23). In particular, we consider the local pressure setup near the areas having abrupt topographic changes. Since the momentum balances are similar for τ_x and τ_y , the momentum balance with respect to τ_x is only presented (Figs. 9, 10, and 12).

The balance between CR and TD is dominant for the inertial currents (first and second columns of Figs. 9 and 10):

$$\frac{\partial \mathbf{u}}{\partial t} + f_c \times \mathbf{u} = 0. \tag{21}$$

The reduced magnitudes of transfer functions at the diurnal frequency near the coast are due to the friction on the coastal boundaries, and the enhanced responses offshore result from the inertial resonance (Fig. 7i–l). Further, the momentum balance near the Coronado Islands shows significance of other terms such as nonlinear terms and pressure gradients:

$$\frac{\partial u}{\partial t} + \mathbf{u} \cdot \nabla u - f_c v = -g \frac{\partial \eta}{\partial x}, \tag{22}$$

$$\frac{\partial v}{\partial t} + \mathbf{u} \cdot \nabla v + f_c u = -g \frac{\partial \eta}{\partial y}. \tag{23}$$

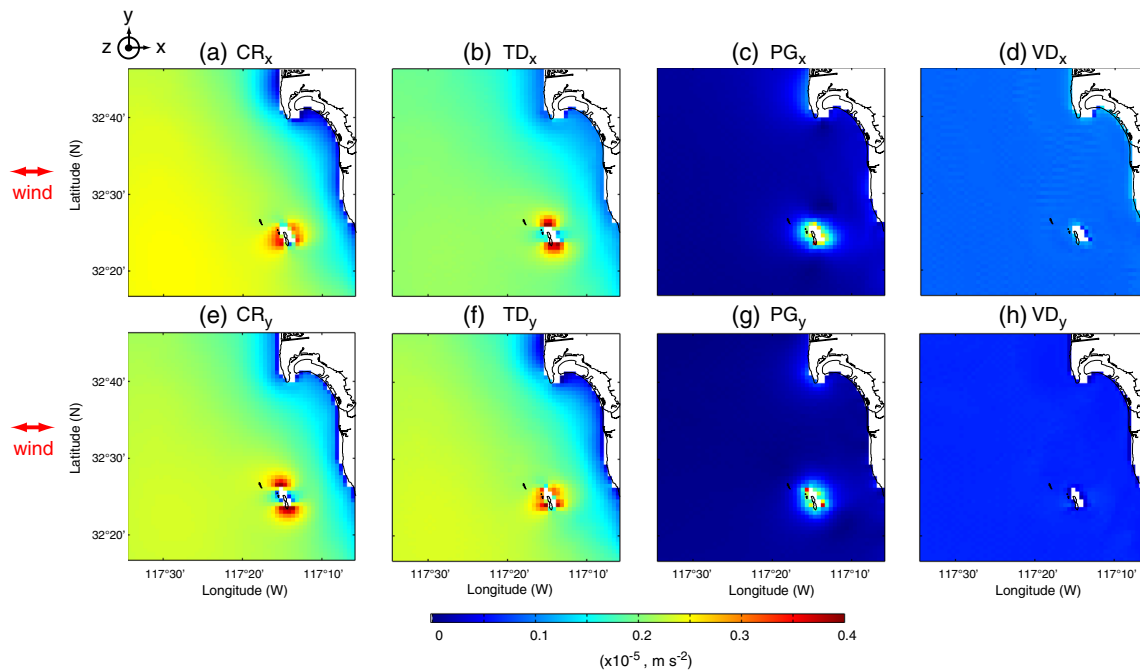


Fig. 9 Magnitudes of Fourier coefficients of CR, TD, PG, and VD terms ($\times 10^5$, m s^{-2}) at the diurnal frequency [$\sigma = \sigma_D$, **i–p**] in the top vertical layer ($z = z_0$). **a–d**: x -directional momentum terms to τ_x . **a** CR_x ($-f_c v$), **b** TD_x ($\partial u / \partial t$), **c** PG_x ($-g \partial \eta / \partial x$), and **d** VD_x ($A_z \partial^2 u / \partial z^2$). **e–h**: y -directional momentum terms to τ_x . **e** CR_y ($f_c u$), **f** TD_y ($\partial v / \partial t$), **g** PG_y ($-g \partial \eta / \partial y$), and **h** VD_y

($A_z \partial^2 v / \partial z^2$). As the magnitudes of CR, TD, PG, and VD terms in the momentum equations to τ_x are identical to the terms to τ_y , the terms to τ_x are only presented. The directions of wind stress are marked on the left of each row. **a–h** share a color bar on the bottom. See Section 3 for convention of subscripts and superscripts

As the number of grid points having significant non-linear terms is less than 2 % of total grid points in the study domain, the linear assumption in the wind-current system can be reasonable (see Section 3 for more details).

In the x -directional momentum balance due to τ_x , the PG and AD terms appear at both east and west sides of the islands with alternative signs (Fig. 10i–p). The VD term is relatively smaller than the other terms (PG, CR, and TD; less than 8 % of the sum of these terms).

Considering the magnitudes of the model-derived SSH responses and the PG terms in the momentum balance at low and diurnal frequencies, the enhanced areas of the SSH response do not always correspond to regions

having dominant PG terms (see Fig. 2q and r, and middle column in Fig. 5 for $\sigma = \sigma_L$; Fig. 7q, r, b, and f for $\sigma = \sigma_D$) because the slopes of SSHs (spatial gradients) at the diurnal and inertial frequencies can be low near the coast.

4.2.3 Influence of seasonal stratification

The model-derived transfer functions and momentum balance shown so far are based on summer stratification (Fig. 11a). The mixed layer depth and characteristics of near-inertial internal oscillations depend on seasonal stratification. To highlight these effects, we present vertical sections showing momentum balances at the inertial frequency for summer and winter (Figs. 11b and 12). The wind

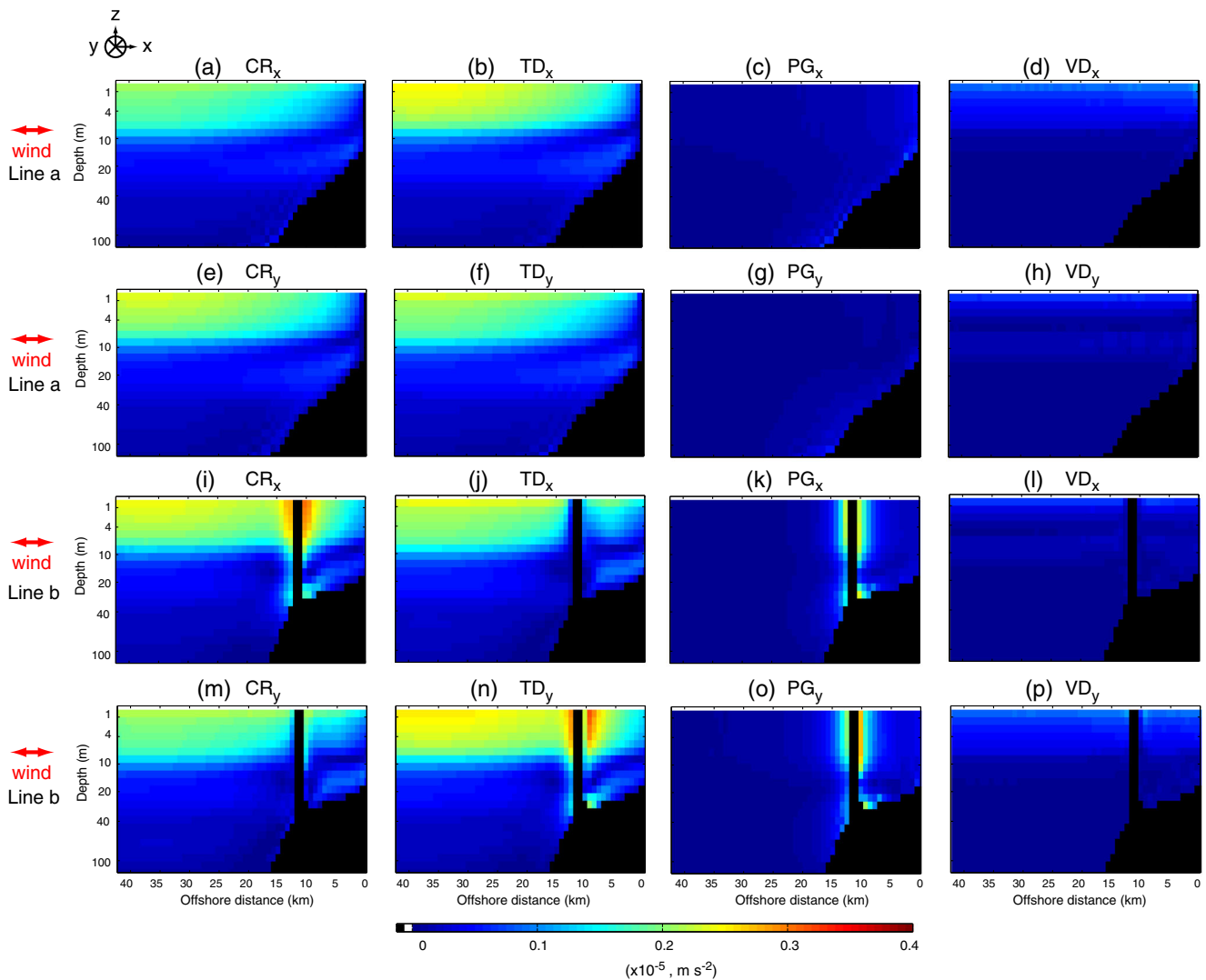


Fig. 10 Magnitudes of Fourier coefficients of CR, TD, PG, and VD terms ($\times 10^5$, m s^{-2}) at the diurnal frequency ($\sigma = \sigma_D$) and along two cross-shore line lines [a–h] for the cross-shore line a and i–p for a cross-shore line b in Fig. 1]. **a–d** and **i–l**: x -directional momentum terms to τ_x . **a** and **i**: CR_x ($-f_c v$). **b** and **f**: TD_x ($\partial u / \partial t$). **c** and **g**: PG_x ($-g \partial \eta / \partial x$). **d** and **l**: VD_x ($A_z \partial^2 v / \partial z^2$). **e–h** and **m–p**: y -directional momentum terms to τ_x . **e** and **m**: CR_y ($f_c u$). **f** and **n**: TD_y ($\partial v / \partial t$). **g**

and **o**: PG_y ($-g \partial \eta / \partial y$). and **h** and **p**: VD_y ($A_z \partial^2 v / \partial z^2$). As the magnitudes of CR, TD, PG, and VD terms in the momentum equations to τ_x are identical to the terms to τ_y , the terms to τ_x are only presented. The directions of wind stress are marked on the left of each row. **a–p** share a colorbar on the bottom. See Section 3 for convention of subscripts and superscripts. Note that the depth is nonlinearly scaled to highlight the feature in the surface layer

responses with high stratification (summer) are stronger and more confined near the surface than those with weak stratification (winter) (e.g., Shearman 2005). This is the same mechanism as for diurnal jets speeding up during the day time (e.g., Price et al. 1986).

In winter (second and fourth rows in Fig. 12) the wind stress divergence penetrates into deeper depth, so the magnitudes of CR and TD (first and second columns in Fig. 12) below the mixed layer are slightly increased. Wind stress at the inertial frequency produces pressure gradients near the islands only during summer stratification (Fig. 12k and o).

4.3 Summary of the transfer function and momentum balance analyses

As a way to identify the dynamical system using the stochastic approach, the transfer function analysis enables us to examine the relationship between driving forces and responses in the frequency domain. In this paper, we provide the dynamical and comprehensive descriptions at three primary frequencies ($\sigma = \sigma_L$, σ_D , and σ_f) using momentum equations and transfer functions, obtained from the observations and the idealized three-dimensional ocean circulation model.

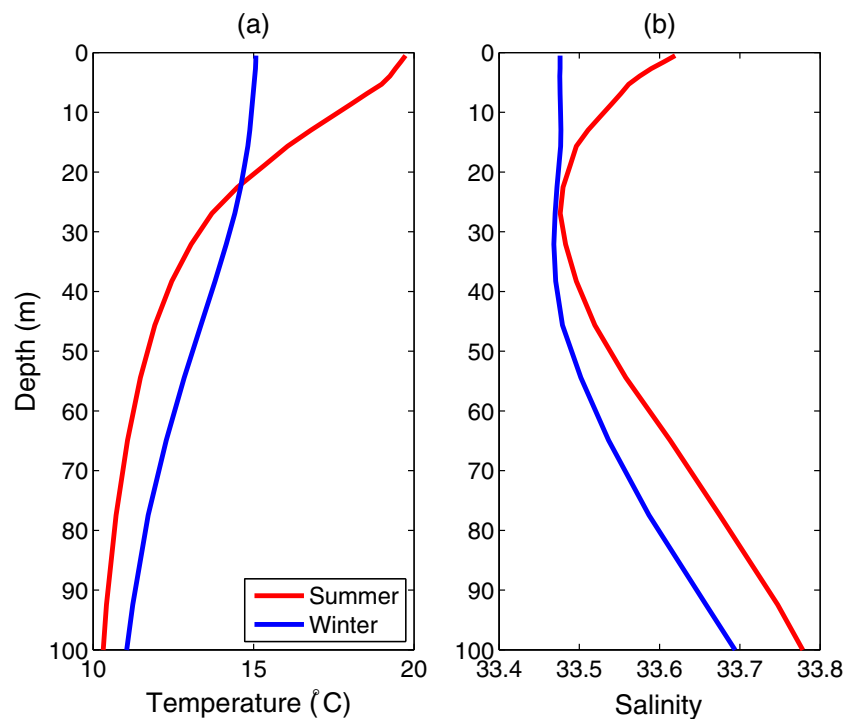
The transfer function analysis highlights that (1) at low frequency, wind stress in the cross-shore and along-shore directions drives nearshore, alongshore near-surface

currents; (2) there is a 180° argument difference between cross-shore winds and along-shore currents; and (3) at diurnal or inertial frequencies, the magnitude of the transfer function is largest offshore, with both downwind and crosswind responses.

The momentum budget analysis summarizes that (1) at low frequency, the surface Ekman balance dominates in the offshore surface mixed layer and geostrophic balance becomes dominant in the nearshore and alongshore currents and (2) at diurnal and inertial frequencies, the inertial dynamics is the primary balance.

As an example of the dynamical interpretation using transfer function analysis, the alongshore surface circulation driven by cross-shore wind stress can be explained in three frequencies. At $\sigma = \sigma_L$, the cross-shore wind stress and along-shore surface currents have nearly 180° argument difference ($\Theta_{yx}^H \approx 180^\circ$; Fig. 2o), which indicates the opposite timings of their maximum and minimum. The argument decreases into 90° as the frequency increases to the diurnal frequency (or near-inertial frequency) [$\Theta_{yx}^H \rightarrow 90^\circ$ as $\sigma \rightarrow \sigma_D$ ($0 < \sigma < \sigma_D$); Fig. 7o] and is abruptly changed into 45° ($\Theta_{yx}^H = 45^\circ$) at $\sigma = \sigma_f$ (see Fig. 1d in Kim et al. (2009b)). While the low-frequency wind stress in the cross-shore direction is relatively weaker than that in the along-shore direction, the circulation in the vicinity of the complex coastline and embayment areas may require to include the influence of the cross-shore wind stress (e.g., Winant 2004; Ponte 2010), which has

Fig. 11 Seasonal **a** temperature ($^\circ\text{C}$) and **b** salinity profiles in the upper 100-m depth observed at C in Fig. 1, which is the one of the CalCOFI stations on the line 93.3, used as initial conditions of the numerical model



received less attention and sometimes even neglected in the coastal circulation studies (e.g., Allen and Smith 1981; Pettigrew 1981; Lentz and Winant 1986; Lee et al. 1989; Lentz et al. 1999).

5 Discussion

5.1 Benefits of the transfer function analysis in understanding shelf dynamics

The transfer function analysis can provide dynamical insights on the shelf dynamics in the frequency domain.

Using horizontal maps of the magnitude of the transfer function, we can identify coastal regions where geostrophic balance or pressure gradients against the boundaries are dominant and their respective spatial scales of influence. Particularly, it can be used to delineate the inner and outer shelf areas in terms of the timescale or frequency band of interest. Moreover, the transfer function analysis on the vertical current profiles and cross-shore transects can provide the effective depth (e.g., inner shelf and outer shelf) of influence of the wind momentum and can explain the fine details of the cross-shore circulation such as how the surface and bottom boundary layers are coherent with surface wind forcing. Additionally, the transfer function analysis has revealed

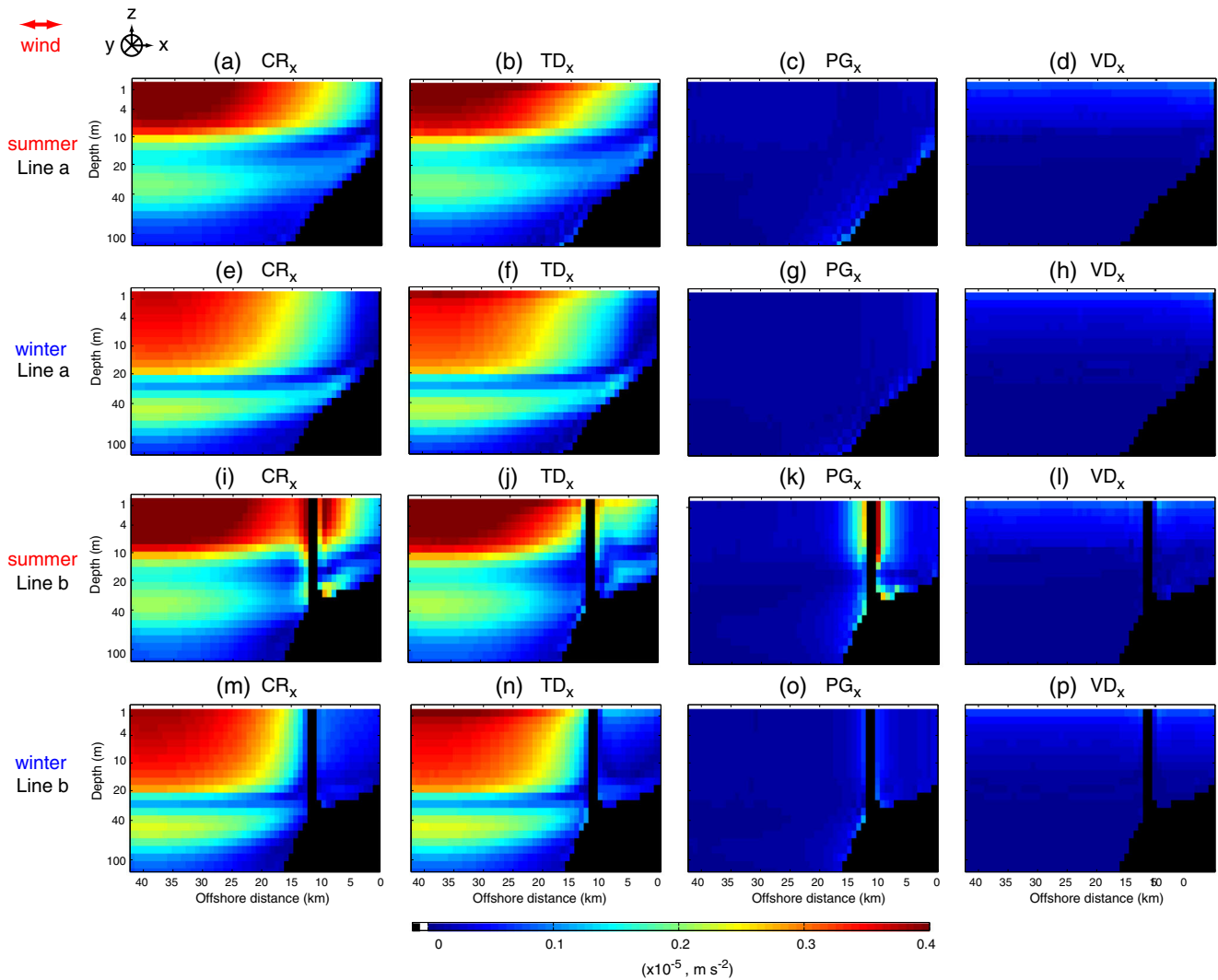


Fig. 12 A comparison of magnitudes of Fourier coefficients of CR, TD, PG, and VD terms ($\times 10^5, \text{m s}^{-2}$) of x -directional momentum balance to τ_x at the inertial frequency ($\sigma = \sigma_f$) and along two cross-shore lines [a–h for a cross-shore line a and i–p for a cross-shore line b in Fig. 1] under seasonal stratification (summer and winter). a–d and i–l: Summer. e–h and m–p: Winter. Columns left to right indicate CR_x ($-f_c v$), TD_x ($\partial u / \partial t$), PG_x ($-g \partial \eta / \partial x$), and VD_x ($A_z \partial^2 u / \partial z^2$). As the

magnitudes of CR, TD, PG, and VD terms in the momentum equations to τ_x are identical to the terms to τ_y , the terms to τ_x are only presented. The direction of wind stress is marked on the left corner and the season is denoted on the left of each row. a–p share a colorbar on the bottom. See Section 3 for convention of subscripts and superscripts. Note that the depth is nonlinearly scaled to highlight the feature in the surface layer

the inertial variance in the sea surface heights forced by winds (e.g., Fig. 11 in Verdy et al. (2013)), which has not been reported in the observations.

The argument of the isotropic transfer function (Appendix C) provides the influence of stratification in the inner shelf and outer shelf areas (e.g., Kim et al. 2010b). In the wind-forced coastal circulation, the veering angle of currents at low frequency in the inner shelf becomes relatively higher than that in the outer shelf due to decreased Ekman spiral under reduced stratification and increased eddy viscosity in the shallow water (e.g., Lentz 2001; Kirincich et al. 2005).

Analytical solutions of both the time-transient (unsteady) Ekman model (e.g., Lewis and Belcher 2004) and frequency-domain Ekman model (e.g., Kim et al. 2009b, 2014) are equivalent, which can be addressed with the outputs from numerical simulations. However, as the transient solutions on coastal upwelling and downwelling (e.g., Austin and Lentz 2002; Allen et al. 1995) contain broadband energy, the transfer function at a specific frequency may not explain the corresponding time-transient solution.

In previous studies of coastal dynamics, the momentum budget analysis has been done using bandpass-filtered time series or using temporal mean of individual momentum terms (e.g., Winant et al. 1987; Dever 1997; Lentz and Trowbridge 2001; Lentz and Chapman 2004; Fewings et al. 2008). The choice of the frequency band for bandpass filtering can be a difficult job to identify the clearly balanced momentum terms. However, the momentum balance analysis in the frequency domain can separate the dominant momentum terms as a function of frequency and help us to isolate the timescales of meaningful terms of the interested dynamics (e.g., Dever 1997; Lentz and Trowbridge 2001). While the time domain analysis can address the time-transient solutions of terms in momentum equations (e.g., Allen et al. 1995; Austin and Lentz 2002), the frequency domain analysis can be more useful in explaining the dynamical terms having periodic and stationary variability at the given frequency or frequency bands. On the contrary, the response function in the time domain, the inversely Fourier-transformed transfer function, can be used to examine the time-transient solutions in coastal dynamics (e.g., Kim et al. 2014). For instance, the wind response function explains the near-inertial oscillations with time decay and geostrophic currents, which correspond to responses of the ocean at rest to the abrupt wind impulse (e.g., Kim et al. 2009b; D'Asaro 1985). Additionally, in the relationship between forcing and response, the response function can address how the local disturbance affects the ocean physics in the entire domain. In the opposite sense, the adjoint model simulates the ocean physics backward to determine which model inputs are responsible for making the perturbation (e.g., Verdy et al. 2013).

5.2 Applications and limitations of the transfer function analysis

In addition, the transfer function analysis can be easily adapted for the interpretation of the limited and under-sampled in situ observations with shelf dynamics. In a similar way, the wind-driven circulation in the bay has been investigated elsewhere (e.g., Winant 2004; Ponte 2010). Besides, the anisotropic transfer function can separate the time lag and veering angle, which are lumped into the argument of the isotropic transfer function. The data-derived isotropic transfer functions at the same three frequencies ($\sigma = \sigma_L, \sigma_D$, and σ_f) (e.g., Kim et al. 2010b) can be compared with the model-derived anisotropic functions (see Appendix D for more details).

The proposed transfer function analysis may not guarantee the dynamically consistent relationship between forcing and response. For instance, while the land/sea breezes and S_1 barotropic tidal currents are not physically coherent and correlated, they can have a statistically coherent relationship. Thus, a dynamical model can be used to identify the limitations of the statistical analysis. In contrast, the simulated ocean states present the existence of wind-driven near-inertial oscillations in the ocean surface and interior. However, the observations of surface and subsurface currents off southern San Diego do not show the significant variance at the inertial frequency, and the statistically coherent relationship related to the inertial currents was not found (e.g., Kim et al. 2009b, 2010b; Kim 2010). Thus, the coastal circulation should be verified and cross-validated with the statistical and dynamical analyses.

In a similar context, there are several areas to have the inconsistent spatial structures in the data-derived and model-derived transfer functions, which can be associated with issues related to the SNR in observations and technical limitations (e.g., the bias in the radar beam pattern and the attenuation of the radar signals with distance). Thus, the numerical simulations can tell us the dynamically consistent three-dimensional field and help us to discern the observational limits and errors which may be imposed in the statistical analysis.

5.3 Relevance with Lerczak et al. (2001)

The wind-driven surface currents at low frequency off southern San Diego have the decorrelation length scales of 60 to 80 km, and the Rossby number relevant to the wind-driven surface circulation is expected to be very small ($R_0 \ll 1$) (Kim et al. 2010a). The continuous in situ ocean observations (ADCP and HFRs) over several years in the study domain do not show the significant near-inertial variance (e.g., Kim et al. 2010a, 2009a; Kim 2010). Specifically, the spectral analysis of surface and subsurface current time

series, which are long enough to isolate the variance at two nearby frequencies—diurnal frequency ($\sigma_D = 1$ cpd) and local inertial frequency ($\sigma_f = 1.07$ cpd), exhibits that the inertial variance is negligible and the variance at two frequencies does not have any evidences for the energy spreading (e.g., cusped peak). Thus, the near-inertial variance is neither significant nor shifted due to background low frequency or mean currents. Although the wind forcing in the model is relatively weak, the simulation at the diurnal frequency produces very weak internal waves compared with the ones at the inertial frequency. Therefore, this paper may not be relevant to Lerczak et al. (2001).

5.4 Mismatch of the scaling factor and length scales

Although the magnitudes of the data-derived and model-derived transfer functions have qualitative similarity in their spatial structure, the observed current responses are larger by nearly a constant factor of 2.5 and have two times larger spatial scales (Figs. 2 and 7).

The scaling factor can be attributed to the bandwidth of transfer functions and the model configuration related to surface mixing. As the data-derived transfer functions are computed from finite Fourier transform (FFT) of time series, the magnitude at a given single frequency represents the value within a finite bandwidth. Meanwhile, the model-derived transfer functions are computed by least-squares fit at the wind forcing frequency such as harmonic analysis for fitting of tidal lines, which does not have a finite bandwidth. Thus, the bandwidth of the model-derived transfer function tends to be smaller than that of the data-derived transfer function. While the scaling factor can be a function of the resolution of the frequency axis, the exact mathematical formulation for the scaling factor may not be derivable. In addition to the above factors affecting the spatial scales of the model- and data-derived transfer functions, the surface and bottom boundary layer dynamics, the choice of the quadratic bottom drag coefficient, and the absence of real atmospheric forcing in this idealized model simulation can possibly contribute to the differences between model- and data-derived transfer functions.

Regarding the mismatch on the spatial scales of the magnitude of the transfer functions, enhanced and larger spatial scales of the magnitude of the data-derived transfer functions might be related to the combined processes due to local and remote winds at synoptic scales as opposed to the spatially uniform local wind forcing in the model. For instance, the features of coastally trapped waves captured in the U.S. West Coast (USWC) HFR network appear within 25 to 50 km from the shoreline over most of the USWC and their persistent and poleward propagations along with sea surface elevations are partially coherent with the large scale wind field (e.g., Kim et al. 2011, 2013). The remote wind

forcing tends to generate broader scale current responses. Moreover, as the model simulations in this study used spatially uniform wind stress which does not contain any spatial structure of wind (e.g., wind shear, wind stress curl), the indirectly forced wind response (e.g., Rykaczewski and Checkley 2008) may not be included in the model.

6 Conclusions

A complementary statistical and dynamical assessment of the wind-driven coastal circulation off southern San Diego has been carried out by analyzing in situ observations of the surface and subsurface currents and the wind data at a local wind station along with numerical model simulations implemented using realistic bottom topography and spatially uniform wind stress forcing. Linear regression between Fourier coefficients of both wind stress and currents provides a transfer function that characterizes the local wind-driven coastal circulation. This statistical estimation of the transfer function gives an alternative approach to describe the system as compared to the dynamical analysis using momentum balance terms in the governing equations. The present study uses anisotropic transfer functions, which allows isolating the current responses corresponding to individual wind directions (zonal and meridional) at three primary frequencies (low, diurnal, and inertial frequencies) to delineate the dominant coastal circulation. This analysis provides two-dimensional maps of horizontal $x - y$ sections and vertical $x - z$ sections of ocean responses to wind forcing, derived purely from observations as well as from idealized ocean model simulations. In addition, the dynamical analysis of momentum balance terms of the model solutions provides the spatial structure of wind-driven pressure gradients and near-inertial motions. Finally, all directional winds and currents at three primary frequencies are taken into consideration.

The magnitudes of transfer functions at low frequency are enhanced near the coast, attributed to geostrophic balance between wind-driven pressure gradients and the Coriolis force on currents. This response diminishes away from the coast, returning to the balance between Coriolis force and friction, as in the classic Ekman model. The transfer functions near the inertial frequency show reduced magnitudes near the coast primarily due to friction in the coastal boundary as opposed to the enhanced response offshore as a result of the inertial resonance. The surface circulation and transfer functions at the diurnal frequency in this area are similar to the inertial ones.

The vertical transects at low frequency show that the dominant momentum balance is the Ekman balance in the upper layer and geostrophic balance in the interior. In addition, surface geostrophic balance appears at the coastal

boundaries. For the diurnal forcing, the internal near-inertial oscillations and alternating pressure setups on either side of the islands with abrupt changes in topography are seen. The seasonal stratification affects the mixed layer depth and the magnitude of wind-driven responses, confining the wind stress divergence near the surface during summer (strong stratification) and allowing it to penetrate deeper during winter (weak stratification).

The anisotropic transfer functions are composed of four components with respect to individual directions of wind stress and currents, and they are transformed into the ISCs and ASCs by their sums and differences. The ISCs and ASCs can be used as a priori to improve the estimate of the data-derived transfer functions, especially, when wind stress and currents in a single direction are poorly determined.

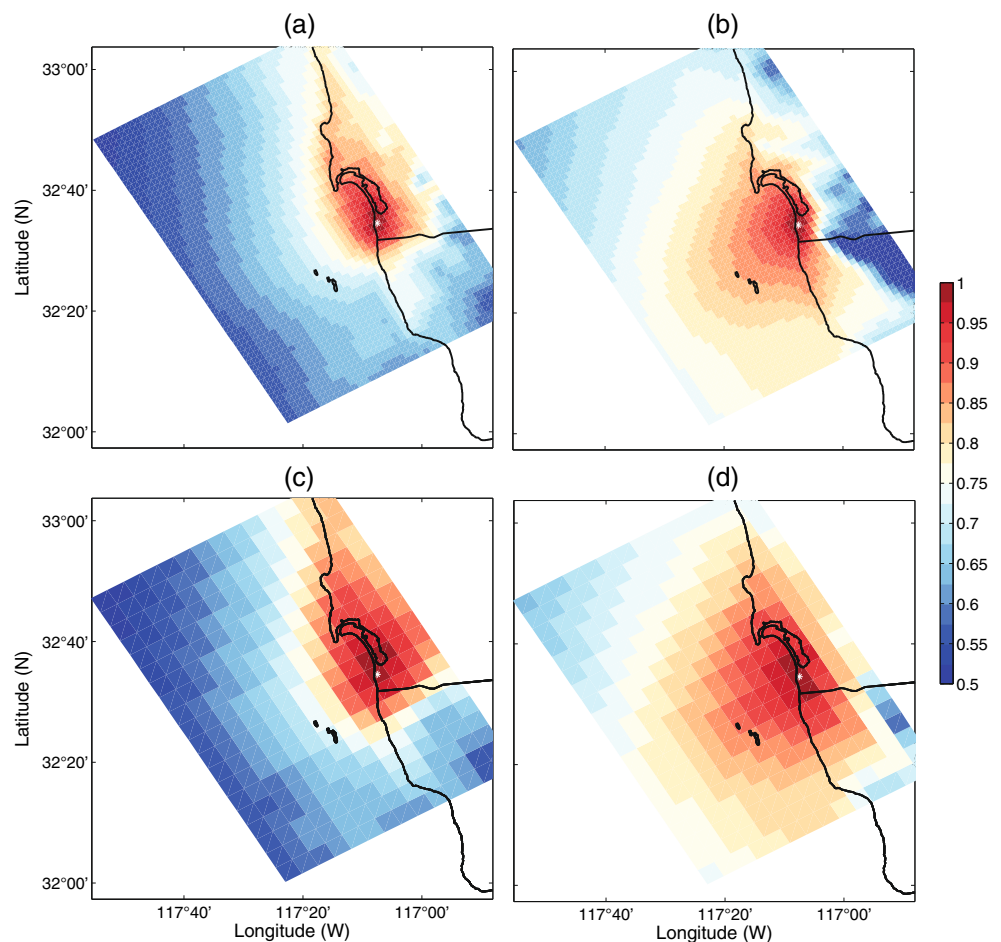
Acknowledgments Sung Yong Kim is supported by the Basic Science Research Program through the National Research Foundation (NRF), Ministry of Education (no. 2013R1A1A2057849), the Human Resources Development of the Korea Institute of Energy Technology Evaluation and Planning (KETEP), Ministry of Trade, Industry

and Energy (no. 20134030200300), and the program on Management of Marine Organisms Causing Ecological Disturbance and Harmful Effects through Korea Integrated Marine Science Technology (KIMST) and Ministry of Fishery (MOF), Republic of Korea. Ganesh Gopalakrishnan and Aurelien Ponte are sponsored by NOAA (NOAA Award NA10OAR4320156). Surface current data are provided from the Southern California Coastal Ocean Observing System (SCCOOS, Available online at <http://www.sccoos.org>) at Scripps Institution of Oceanography. Wind data at the Tijuana River (Tidal Linkage) are maintained by the System-Wide Monitoring Program at the Tijuana River National Estuarine Research Reserve, Estuarine Reserves Division (TRNERR), NOAA, Centralized Data Management Office (CDMO), Baruch Marine Field Lab, and University of South Carolina. The bathymetry is provided by National Geophysical Data Center (NGDC). The authors thank B. D. Cornuelle for providing ideas and a chance to generate synergy among coauthors and E. Terrill for providing the data.

Appendix A: Spatial scales of the surface wind field

The decorrelation length scales of the surface wind field off southern San Diego are examined with the COAMPS nowcast data with two spatial resolutions of 1.7 and 5.1 km

Fig. 13 An example of spatial correlations of the COAMPS hourly nowcast wind data at W (a white asterisk in Fig. 1. **a** and **c**: $\rho_{uu}(\mathbf{x}, \mathbf{x}')$. **b** and **d**: $\rho_{vv}(\mathbf{x}, \mathbf{x}')$. **a** and **b**: 1.7 km resolution. **b** and **d**: 5.1 km resolution



(Hodur 1997). An example of spatial correlations of the hourly model wind at W in Fig. 1 for one year (2006) is shown in Fig 13. The length scales are asymmetric, i.e., relatively long seaward and short shoreward, in the range of 25 to 120 km.

Appendix B: Equilibrium of the model solutions

An example of model currents forced by low-frequency cross-shore wind stress (τ_x) is presented with the hourly time series of u - and v -components at the center of a cross-shore line a in Fig. 1 and the surface layer ($z = -0.5$ m) over 30 days (Fig. 14a and b). The data for the first three days are excluded (a black box), and the rest of model solutions is used for the transfer function analysis and momentum budget analysis. Although the weak near-inertial oscillations are still imposed in the time series after three days, the model solutions at low frequency reach the equilibrium quickly.

Appendix C: Isotropic subsurface transfer function

From the isotropic relationship (Eq. 4), the wind-coherent currents are as follows:

$$\hat{u}_W(z, \sigma) = E(z, \sigma) [\hat{\tau}_x(\sigma) + i\hat{\tau}_y(\sigma)], \tag{24}$$

$$= [E_r(z, \sigma) + iE_i(z, \sigma)] [\hat{\tau}_x(\sigma) + i\hat{\tau}_y(\sigma)], \tag{25}$$

where E_r and E_i indicate the real and imaginary parts of the isotropic transfer function (E). The corresponding

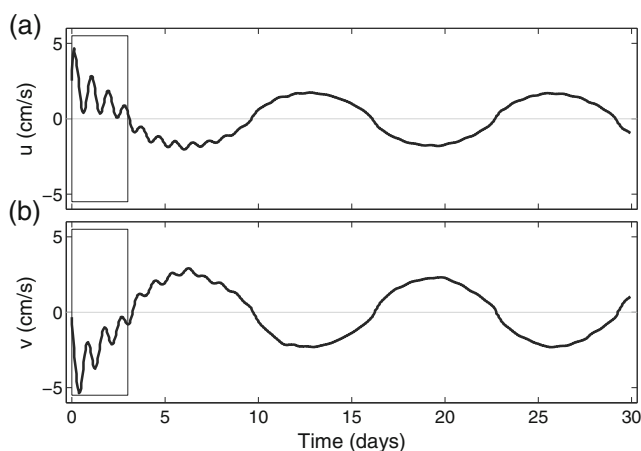


Fig. 14 The hourly time series of model currents, forced by low-frequency wind stress in the cross-shore direction (τ_x), at the center of a cross-shore line a in Fig. 1 and the surface layer ($z = -0.5$ m) over 30 days. The data for the first three days are excluded (a black box), and the rest of model solutions is used for the transfer function analysis. **a** u -component (cm s^{-1}), **b** v -component (cm s^{-1})

magnitude and argument are referred to as E and Θ^E , respectively, i.e.,

$$E = |E| = |E_r + iE_i|, \tag{26}$$

$$\Theta^E = \tan^{-1} \frac{E_i}{E_r}, \tag{27}$$

The data-derived isotropic transfer function (E) is computed from the TJR wind stress and the detided HFR surface and ADCP subsurface currents (Fig. 15a and c). The model-derived isotropic transfer function (F) is based on the Ekman model (Fig. 15b and d) (e.g., Kim et al. 2009b).

The peak near the inertial frequency decreases with depth, consistent with the model, penetrating up to about 8 m. However, the significant variance at low frequency does not appear in the model, which indicates the influence of pressure gradients near the coast because the Ekman model does not include pressure gradient terms (Fig. 15a and b) (e.g., Kim et al. 2009b). The arguments of data- and model-derived transfer functions are very similar except for the sign shift at the zero frequency (Fig. 15c and d).

Appendix D: Time lag and veering angle

As the argument (Θ^E) of the isotropic transfer function (E in Eq. 24) contains the time lag (α) and veering angle (β), i.e., $\Theta^E = \alpha + \beta$ (see Kim et al. (2009b)),

$$\hat{u}(\sigma) + i\hat{v}(\sigma) = E(\sigma)e^{i\Theta^E(\sigma)} [\hat{\tau}_x(\sigma) + i\hat{\tau}_y(\sigma)], \tag{28}$$

we can separate them with the relationship between individual components of wind stress and currents, i.e., anisotropic transfer functions.

As a simple case when ISCs are dominant over ASCs (e.g., offshore region), the anisotropic transfer functions can be paired ($H_{xx} = H_{yy}$ and $H_{xy} = -H_{yx}$) (e.g., Kim et al. 2009b). The Fourier coefficients of currents are expressed with the isotropic convention:

$$\hat{u} + i\hat{v} = (H_{xx}\hat{\tau}_x + H_{xy}\hat{\tau}_y) + i(H_{yx}\hat{\tau}_x + H_{yy}\hat{\tau}_y), \tag{29}$$

$$= \left(|H_{xx}|e^{i\Theta_{xx}^H}\hat{\tau}_x + |H_{xy}|e^{i\Theta_{xy}^H}\hat{\tau}_y \right) + i \left(|H_{xy}|e^{i(\Theta_{xy}^H + \pi)}\hat{\tau}_x + |H_{xx}|e^{i\Theta_{xx}^H}\hat{\tau}_y \right), \tag{30}$$

$$= \left(|H_{xx}|e^{i\Theta_{xx}^H} - i|H_{xy}|e^{i\Theta_{xy}^H} \right) (\hat{\tau}_x + i\hat{\tau}_y), \tag{31}$$

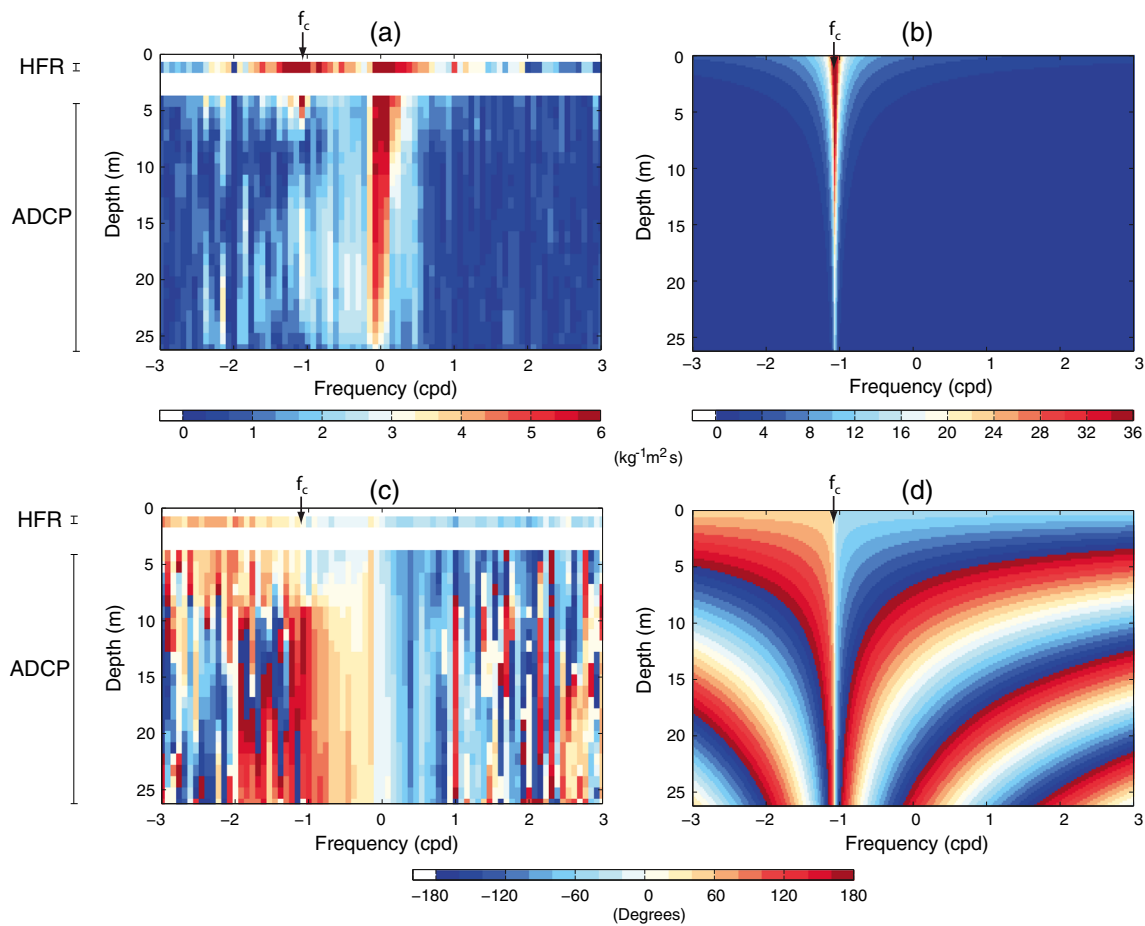


Fig. 15 Magnitudes and arguments of surface and subsurface isotropic transfer functions derived from HFRs and ADCP observations at T in Fig. 1 and the Ekman model. **a** E , **b** F , **c** Θ^E , and **d** Θ^F .

f_c and δ_E denote the local inertial frequency (1.07 cpd) and the Ekman depth ($\delta_E = \pi\sqrt{2\nu/f_c} = 8.705$ m, where $\nu = 3 \times 10^{-4} \text{ m}^2 \text{ s}^{-1}$ is the kinematic viscosity), respectively

where H_{xx} has the zero veering angle and the time lag of Θ_{xx}^H ($\alpha = \Theta_{xx}^H$ and $\beta = 0^\circ$), and H_{xy} has the veering angle of -90° and the time lag of Θ_{xy}^H ($\alpha = \Theta_{xy}^H$ and $\beta = -90^\circ$). Thus, this comparison enables us to differentiate the veering angle and time lag when the argument is ambiguously computed under the isotropic assumption such as complex coherence and correlation.

At $\sigma = \sigma_L$, Θ_{xx}^H is in the range of -2° to -5° , and Θ_{xy}^H is in the range of -7° to -8° (Fig. 2m–p; Eq. 31). The estimated time lag (α) and veering angle (β) for three cases of the argument (Θ^E) at low frequency ($\Theta^E = -30^\circ, -45^\circ$, and -60°) (e.g., Kim et al. 2010b) are shown in Table 1. For the case of $\sigma = 0$ cpd (Ekman model), the time lag and veering angle are zero and -45° , respectively.

At $\sigma = \sigma_D$, Θ_{xx}^H is in the range of 2° to 6° , and Θ_{xy}^H is in the range of -61° to -67° (Fig. 7m–7p). The estimated time lag (α) and veering angle (β) for four cases of the argument (Θ^E) at the diurnal frequency ($\Theta^E = -30^\circ, -45^\circ, -60^\circ$, and -75°) (e.g., Kim et al. 2010b) are shown in Table 2

Appendix E: Estimates of ISCs and ASCs

Equations 14 and 15 are solved together frequency by frequency (e.g., Wunsch 1996; Kim 2009):

$$\begin{bmatrix} \hat{u} \\ \hat{v} \end{bmatrix} = \begin{bmatrix} \hat{\tau}_x & \hat{\tau}_y & \hat{\tau}_x & \hat{\tau}_y \\ \hat{\tau}_y & -\hat{\tau}_x & -\hat{\tau}_y & \hat{\tau}_x \end{bmatrix} \begin{bmatrix} I_d \\ I_c \\ A_d \\ A_c \end{bmatrix}, \tag{32}$$

where \hat{u} , \hat{v} , $\hat{\tau}_x$, and $\hat{\tau}_y$ are column vectors consisting of N sub-sampled Fourier coefficients at a single frequency (\dagger is the vector transpose), presented as follows:

$$\hat{u} = [\hat{u}_1 \hat{u}_2 \cdots \hat{u}_N]^\dagger, \tag{33}$$

$$\hat{v} = [\hat{v}_1 \hat{v}_2 \cdots \hat{v}_N]^\dagger, \tag{34}$$

$$\hat{\tau}_x = [\hat{\tau}_{x1} \hat{\tau}_{x2} \cdots \hat{\tau}_{xN}]^\dagger, \tag{35}$$

$$\hat{\tau}_y = [\hat{\tau}_{y1} \hat{\tau}_{y2} \cdots \hat{\tau}_{yN}]^\dagger. \tag{36}$$

Equation 32 is formulated as

$$\mathbf{d} = \mathbf{Z} \mathbf{m}, \tag{37}$$

Table 1 Estimates of the time lag (α , degrees or hours) and veering angle (β , degrees) for three cases of the argument ($\Theta^E = \alpha + \beta$) of the isotropic transfer function at low frequency ($\sigma = \sigma_L$) using the pairs of time lags (Θ_{xx}^H or Θ_{xy}^H) and veering angles (0° or -90°) of the anisotropic transfer functions. The negative time lag indicates that wind stress leads the currents, and the negative veering angle measures the amount of turn that the currents head to the right of the wind direction

Cases	Θ^E	-30°	-45°	-60°
Summer	α	-4.2° (-3.65 h)	-5.0° (-4.34 h)	-5.8° (-5.04 h)
	β	-25.8°	-40.0°	-54.2°
Winter	α	-6.0° (-5.25 h)	-6.6° (-5.73 h)	-7.2° (-6.26 h)
	β	-24.0°	-38.4°	-52.8°
Ekman	α		0° (0 h)	
	β		-45°	

where \mathbf{d} , \mathbf{Z} , and \mathbf{m} correspond to the currents, wind stress, and isotropy and anisotropy components. The estimated model coefficients ($\hat{\mathbf{m}}$) are

$$\hat{\mathbf{m}} = \mathbf{PZ}^\dagger (\mathbf{ZPZ}^\dagger + \mathbf{R})^{-1} \mathbf{d}, \tag{38}$$

$$= (\mathbf{Z}^\dagger \mathbf{R}^{-1} \mathbf{Z} + \mathbf{P}^{-1})^{-1} \mathbf{Z}^\dagger \mathbf{R}^{-1} \mathbf{d}, \tag{39}$$

where \mathbf{P} and \mathbf{R} are the model and error covariance matrices († is the matrix transpose).

When the error covariance matrix (\mathbf{R}) is replaced with an identity matrix (\mathbf{I}), the model covariance matrix (\mathbf{P}) will become a unique factor to adjust the inverse of SNR (\mathbf{RP}^{-1} ;

Table 2 Estimates of the time lag (α , degrees or hours) and veering angle (β , degrees) for four cases of the argument ($\Theta^E = \alpha + \beta$) of the isotropic transfer function at the diurnal frequency ($\sigma = \sigma_D$) using the pairs of time lags (Θ_{xx}^H or Θ_{xy}^H) and veering angles (0° or -90°) of the anisotropic transfer functions. The meaning of the time lag and the convention of the veering angle are noted in Table 1

Cases	Θ^E	-30°	-45°	-60°	-75°
Summer	α	-10.5° (0.68 h)	-17.2° (-1.13 h)	-23.9° (-1.6 h)	-30.6° (-2 h)
	β	-19.4°	-27.8°	-36.1°	-44.4°
Winter	α	-10.9° (0.68 h)	-17.1° (-1.13 h)	-23.4° (-1.6 h)	-29.6° (-2 h)
	β	-19.1°	-27.9°	-36.6°	-45.4°

$\beta_k, k = 1, 2, 3,$ and 4), whose diagonal components reflect the contribution of each basis function:

$$\mathbf{P} = \begin{bmatrix} \beta_1 & 0 & 0 & 0 \\ 0 & \beta_2 & 0 & 0 \\ 0 & 0 & \beta_3 & 0 \\ 0 & 0 & 0 & \beta_4 \end{bmatrix}. \tag{40}$$

The inverse of SNR for the estimates of ISCs and ASCs is assumed as 0.1, 0.1, 0.5, and 0.5 of the mean eigenvalues of the covariance matrix Fourier coefficients of wind stress, respectively, for $\mathbf{l}_d, \mathbf{l}_c, \mathbf{A}_d,$ and \mathbf{A}_c at the given three frequencies ($\sigma = \sigma_L, \sigma_D,$ and σ_f). The chosen ratios are less sensitive to the overall results.

References

Adcroft A, Campin J, Dutkiewicz S, Evangelinos C, Ferreira D, Forget G, Fox-Kemper B, Heimbach P, Hill C, Hill E (2014) MITgcm user manual. MIT Department of EAPS, Cambridge

Allen JS (1980) Models of wind-driven currents on the continental shelf. *Annu Rev Fluid Mech* 12:389–433. doi:10.1146/annurev.fl.12.010180.002133

Allen JS, Smith RL (1981) On the dynamics of wind-driven shelf currents. *Philos Trans Roy Soc London Ser A Math Phys Sci* 302(1472):617–634. doi:10.1098/rsta.1981.0187

Allen J, Newberger P, Federiuk J (1995) Upwelling circulation on the Oregon continental shelf. Part I: Response to idealized forcing. *J Phys Oceanogr* 25:1843–1866

Austin J, Lentz S (2002) The inner shelf response to wind-driven upwelling and downwelling. *J Phys Oceanogr* 32(7):2171–2193

Brink KH (1991) Coastal-trapped waves and wind-driven currents over the continental shelf. *Annu Rev Fluid Mech* 23:389–412. doi:10.1146/annurev.fl.23.010191.002133

Brink K, Halpern D, Smith R (1980) Circulation in the Peruvian upwelling system near 15°S . *J Geophys Res* 85(C7):4036–4048

Castelao RM, Barth JA (2005) Coastal ocean response to summer upwelling favorable winds in a region of alongshore bottom topography variations off Oregon. *J Geophys Res* 110:C10S04. doi:10.1029/2004JC002409

Chen C, Reid R, Nowlin W (1996) Near-inertial oscillations over the Texas-Louisiana shelf. *J Geophys Res* 101(C2):3509–3524. doi:10.1029/95JC03395

Craig PD (1988) Space and time scales in shelf circulation modelling. *Cont Shelf Res* 8(11):1221–1246

Craig PD (1989) Constant-eddy-viscosity models of vertical structure forced by periodic winds. *Cont Shelf Res* 9(4):343–358

Crawford GB, Large WG (1996) A numerical investigation of resonant inertial response of the ocean to wind forcing. *J Phys Oceanogr* 26(6):873–891

D’Asaro EA (1985) The energy flux from the wind to the near-inertial motions in the surface mixed layer. *J Phys Oceanogr* 15(8):1043–1059

Davies AM (2003) On the interaction between internal tides and wind-induced near-inertial currents at the shelf edge. *J Geophys Res* 108(C3):3099. doi:10.1029/2002JC001375

Davies A, Xing J (2003) Processes influencing wind-induced current profiles in near coastal stratified regions. *Cont Shelf Res* 23 (14–15):1379–1400. doi:10.1016/S0278-4343(03)00119-5

Davis RE, Bogden PS (1989) Variability on the California shelf forced by local and remote winds during the Coastal

- Ocean Dynamics Experiment. *J Geophys Res* 94(C4):4763–4783. doi:[10.1029/JC094iC04p04763](https://doi.org/10.1029/JC094iC04p04763)
- Dever E (1997) Wind-forced cross-shelf circulation on the northern California shelf. *J Phys Oceanogr* 27(8):1566–1580
- Edwards C, Fake T, Bogden P (2004a) Spring-summer frontogenesis at the mouth of Block Island Sound: 1. A numerical investigation into tidal and buoyancy-forced motion. *J Geophys Res* 109:C12021. doi:[10.1029/2003JC002132](https://doi.org/10.1029/2003JC002132)
- Edwards C, Fake T, Codiga D, Bogden P (2004b) Spring-summer frontogenesis at the mouth of Block Island Sound: 2. Combining acoustic Doppler current profiler records with a general circulation model to investigate the impact of subtidal forcing. *J Geophys Res* 109:C12022. doi:[10.1029/2003JC002133](https://doi.org/10.1029/2003JC002133)
- Ekman VW (1905) On the influence of the Earth's rotation on ocean-currents. *Ark Mat Astron Fys* 2:1–53
- Eliot S, Gille ST (2009) Ekman layers in the Southern Ocean: spectral models and observations, vertical viscosity and boundary layer depth. *Ocean Sci* 5:115–139. <http://www.ocean-sci.net/5/115/2009/>
- Emery WJ, Thomson RE (1997) Data analysis methods in physical oceanography. Elsevier, Boston
- Fewings M, Lentz S, Fredericks J (2008) Observations of cross-shelf flow driven by cross-shelf winds on the inner continental shelf. *J Phys Oceanogr* 38(11):2358–2378. doi:[10.1175/2008JPO3990.1](https://doi.org/10.1175/2008JPO3990.1)
- Fukumori I, Lee T, Cheng B, Menemenlis D (2004) The origin, pathway, and destination of Niño-3 water estimated by a simulated passive tracer and its adjoint. *J Phys Oceanogr* 34:582–604
- Gill AE (1982) Atmosphere-ocean dynamics, international geophysics series, vol. 30. Academic, San Diego
- Gonella J (1972) A rotary-component method for analysis in meteorological and oceanographic vector time series. *Deep Sea Res* 19:833–846
- Gopalakrishnan G, Cornuelle BD, Hoteit I (2013a) Adjoint sensitivity studies of Loop current and eddy shedding in the Gulf of Mexico. *J Geophys Res* 118(7):3315–3335. doi:[10.1002/jgrc.20240](https://doi.org/10.1002/jgrc.20240)
- Gopalakrishnan G, Cornuelle BD, Hoteit I, Rudnick DL, Owens WB (2013b) State estimates and forecasts of the Loop current in the Gulf of Mexico using the MITgcm and its adjoint. *J Geophys Res* 118(7):3292–3314. doi:[10.1002/jgrc.20239](https://doi.org/10.1002/jgrc.20239)
- Hodur RM (1997) The Naval Research Laboratory's Coupled Ocean/Atmosphere Mesoscale Prediction System (COAMPS). *Mon Wea Rev* 125:1414–1430
- Hoteit I, Cornuelle B, Kim SY, Forget G, Kohl A, Terrill E (2009) Assessing 4D-VAR for dynamical mapping of coastal high-frequency radar in San Diego. *Dyn Atmos Oceans* 48:175–197. doi:[10.1016/j.dynatmoce.2008.11.005](https://doi.org/10.1016/j.dynatmoce.2008.11.005)
- Hoteit I, Cornuelle B, Heimbach P (2010) An eddy permitting variational data assimilation system for estimating the of the tropical Pacific. *J Geophys Res* 115:C03001. doi:[10.1029/2009JC005347](https://doi.org/10.1029/2009JC005347)
- Hoteit I, Hoar T, Gopalakrishnan G, Collins N, Anderson J, Cornuelle B, Heimbach P (2013) A MITgcm/DART ensemble analysis and prediction system with application to the Gulf of Mexico. *Dyn Atmos Oceans* 63:1–12. doi:[10.1016/j.dynatmoce.2013.03.002](https://doi.org/10.1016/j.dynatmoce.2013.03.002)
- Kim SY (2009) Coastal ocean studies in southern San Diego using high-frequency radar derived surface currents. Ph.D. thesis. Scripps Institution of Oceanography Technical Report. <http://escholarship.org/uc/item/2z5660f4>
- Kim SY (2010) Observations of submesoscale eddies using high-frequency radar-derived kinematic and dynamic quantities. *Cont Shelf Res* 30:1639–1655. doi:[10.1016/j.csr.2010.06.011](https://doi.org/10.1016/j.csr.2010.06.011)
- Kim SY (2014) A statistical description on the wind-coherent responses of sea surface heights off the U.S. West Coast. *Ocean Dyn* 64(1):29–46. doi:[10.1007/s10236-013-0668-3](https://doi.org/10.1007/s10236-013-0668-3)
- Kim SY, Terrill EJ, Cornuelle BD (2008) Mapping surface currents from HF radar radial velocity measurements using optimal interpolation. *J Geophys Res* 113:C10023. doi:[10.1029/2007JC004244](https://doi.org/10.1029/2007JC004244)
- Kim SY, Terrill EJ, Cornuelle BD (2009a) Assessing coastal plumes in a region of multiple discharges: The U.S.–Mexico border. *Environ Sci Technol* 43(19):7450–7457. doi:[10.1021/es900775p](https://doi.org/10.1021/es900775p)
- Kim SY, Cornuelle BD, Terrill EJ (2009b) Anisotropic response of surface currents to the wind in a coastal region. *J Phys Oceanogr* 39(6):1512–1533. doi:[10.1175/2009JPO4013.1](https://doi.org/10.1175/2009JPO4013.1)
- Kim SY, Terrill EJ, Cornuelle BD, Jones B, Washburn L, Moline MA, Paduan JD, Garfield N, Largier JL, Crawford G, Kosro PM (2011) Mapping the U.S. West Coast surface circulation: A multiyear analysis of high-frequency radar observations. *J Geophys Res* 116:C03011. doi:[10.1029/2010JC006669](https://doi.org/10.1029/2010JC006669)
- Kim SY, Cornuelle BD, Terrill EJ (2010a) Decomposing observations of high-frequency radar derived surface currents by their forcing mechanisms: Decomposition techniques and spatial structures of decomposed surface currents. *J Geophys Res* 115:C12007. doi:[10.1029/2010JC006222](https://doi.org/10.1029/2010JC006222)
- Kim SY, Cornuelle BD, Terrill EJ (2010b) Decomposing observations of high-frequency radar derived surface currents by their forcing mechanisms: Locally wind-driven surface currents. *J Geophys Res* 115:C12046. doi:[10.1029/2010JC006223](https://doi.org/10.1029/2010JC006223)
- Kim SY, Cornuelle BD, Terrill EJ, Jones B, Washburn L, Moline MA, Paduan JD, Garfield N, Largier JL, Crawford G, Kosro PM (2013) Poleward propagating subinertial alongshore surface currents off the U.S. West Coast. *J Geophys Res* 118(12):6791–6806. doi:[10.1002/jgrc.20400](https://doi.org/10.1002/jgrc.20400)
- Kim SY, Kosro PM, Kurapov AL (2014) Evaluation of directly wind-coherent near-inertial surface currents off Oregon using a statistical parameterization and analytical models. *J Geophys Res* 119. doi:[10.1002/2014JC010115](https://doi.org/10.1002/2014JC010115)
- Kirincich AR, Barth JA, Grantham BA, Menge BA, Lubchenco J (2005) Wind-driven inner-shelf circulation off central Oregon during summer. *J Geophys Res* 110:C10S03. doi:[10.1029/2004JC002611](https://doi.org/10.1029/2004JC002611)
- Kohl ADS, Cornuelle B (2007) Interannual to decadal changes in the ECCO global synthesis. *J Phys Oceanogr* 37:313–337. doi:[10.1175/JPO3014.1](https://doi.org/10.1175/JPO3014.1)
- Large W, McWilliams J, Doney S (1994) Oceanic vertical mixing: A review and a model with a non-local boundary layer parameterization. *Rev Geophys* 32(4):363–403. doi:[10.1029/94RG01872](https://doi.org/10.1029/94RG01872)
- Lee T, Williams E, Wang J, Evans R, Atkinson L (1989) Response of South Carolina continental shelf waters to wind and Gulf Stream forcing during winter of 1986. *J Geophys Res* 94(C8):10,715–10,754. doi:[10.1029/JC094iC08p10715](https://doi.org/10.1029/JC094iC08p10715)
- Legg S, Hallberg R, Girton J (2006) Comparison of entrainment in overflows simulated by z-coordinate, isopycnal and non-hydrostatic models. *Ocean Model* 11(1–2):69–97. doi:[10.1016/j.ocemod.2004.11.006](https://doi.org/10.1016/j.ocemod.2004.11.006)
- Lentz SJ (1995) Sensitivity of the inner-shelf circulation to the form of the eddy viscosity profile. *J Phys Oceanogr* 25(1):19–28
- Lentz SJ (2001) The influence of stratification on the wind-driven cross-shelf circulation over the North Carolina shelf. *J Phys Oceanogr* 31:2749–2760
- Lentz SJ, Winant CD (1986) Subinertial currents on the southern California shelf. *J Phys Oceanogr* 16:1737–1750
- Lentz SJ, Trowbridge J (2001) A dynamical description of fall and winter mean current profiles over the northern California shelf. *J Phys Oceanogr* 31:914–931

- Lentz SJ, Chapman DC (2004) The importance of non-linear cross-shelf momentum flux during wind-driven coastal upwelling. *J Phys Oceanogr* 34:2444–2457. doi:[10.1175/JPO2644.1](https://doi.org/10.1175/JPO2644.1)
- Lentz S, Fewings M (2012) The wind-and wave-driven inner-shelf circulation. *Annu Rev Mar Sci*:317–343. doi:[10.1146/annurevmarine-120709-142745](https://doi.org/10.1146/annurevmarine-120709-142745)
- Lentz SJ, Guza R, Elgar S, Feddersen F, Herbers T (1999) Momentum balances on the North Carolina inner shelf. *J Geophys Res* 104:18,205–18,226. doi:[10.1029/1999JC900101](https://doi.org/10.1029/1999JC900101)
- Lentz SJ, Trowbridge J (2001) A dynamical description of fall and winter mean current profiles over the northern California shelf. *J Phys Oceanogr* 31:914–931
- Lerczak JA, Hendershott MC, Winant CD (2001) Observations and modeling of coastal internal waves driven by a diurnal sea breeze. *J Geophys. Res.* 106(C9):19,715–19,729
- Lewis DM, Belcher SE (2004) Time-dependent, coupled, Ekman boundary layer solutions incorporating Stokes drift. *Dyn Atmos Oceans* 37:313–351. doi:[10.1016/j.dynatmoce.2003.11.001](https://doi.org/10.1016/j.dynatmoce.2003.11.001)
- Madsen OS (1977) A realistic model of the wind-induced Ekman boundary layer. *J Phys Oceanogr* 7:248–255
- Marshall J, Adcroft A, Hill C, Perelman L, Heisey C (1997) A finite-volume, incompressible Navier Stokes model for studies of the ocean on parallel computers. *J Geophys Res* 102(C3):5753–5766. doi:[10.1029/96JC02775](https://doi.org/10.1029/96JC02775)
- Menemenlis D, Fukumori I, Lee T (2005) Using Green's functions to calibrate an ocean general circulation model. *Mon Wea Rev* 133(5):1224–1240. doi:[10.1175/MWR2912.1](https://doi.org/10.1175/MWR2912.1)
- Millero FJ, Poisson A (1981) International one-atmosphere equation of state of seawater. *Deep Sea Res* 28A(6):625–629
- Millot C, Crepon M (1981) Inertial oscillations on the continental shelf of the Gulf of Lions: Observations and theory. *J Phys Oceanogr* 11:639–657
- Oppenheim AV, Schaffer RW, Buck JR (1998) Discrete-time signal processing, 2nd edn. Prentice Hall Signal Processing Series. Prentice-Hall, Inc., Upper Saddle River, NJ
- Pettigrew NR (1981) The dynamics and kinematics of the coastal boundary layer off Long Island. Ph.D. thesis, Massachusetts Institute of Technology. Dept. of Meteorology and Physical Oceanography. <http://hdl.handle.net/1721.1/27913>
- Pollard RT, Millard RC (1970) Comparison between observed and simulated wind-generated inertial oscillations. *Deep Sea Res* 17:813–821
- Ponte ALS (2010) Periodic wind-driven circulation in an elongated and rotating basin. *J Phys Oceanogr* 40:2043–2058. doi:[10.1175/2010JPO4235.1](https://doi.org/10.1175/2010JPO4235.1)
- Price JF, Weller RA, Pinkel R (1986) Diurnal cycling: Observations and models of the upper ocean response to diurnal heating, cooling, and wind mixing. *J Geophys Res* 91(C7):8411–8427. doi:[10.1029/JC091iC07p08411](https://doi.org/10.1029/JC091iC07p08411)
- Pringle JM (2002) Enhancement of wind-driven upwelling and downwelling by alongshore bathymetric variability. *J Phys Oceanogr* 32:3101–3112
- Rio MH, Hernandez F (2003) High-frequency response of wind-driven currents measured by drifting buoy and altimetry over the World Ocean. *J Geophys Res* 108(C8):3238. doi:[10.1029/2002JC001655](https://doi.org/10.1029/2002JC001655)
- Rykaczewski R, Checkley D (2008) Influence of ocean winds on the pelagic ecosystem in upwelling regions. *Proc Natl Acad Sci* 105(6):1965–1970. doi:[10.1073/pnas.0711777105](https://doi.org/10.1073/pnas.0711777105)
- Shay LK, Lee TN, Williams EJ, Graber HC, Rooth CGH (1998) Effects of low-frequency current variability on near-inertial sub-mesoscale vortices. *J. Geophys. Res.* 103(C9):18,691–18,714. doi:[10.1029/98JC01007](https://doi.org/10.1029/98JC01007)
- Shearman RK (2005) Observations of near-inertial current variability on the New England shelf. *J Geophys Res* 110:C02012. doi:[10.1029/2004JC002341](https://doi.org/10.1029/2004JC002341)
- Shen CY, Evans TE (2001) Surface-to-subsurface velocity projection for shallow water currents. *J Geophys Res* 106(C4):6973–6984. doi:[10.1029/2000JC000267](https://doi.org/10.1029/2000JC000267)
- Stammer D, Wunsch C, Giering R, Eckert C, Heimbach P, Marotzke J, Adcroft A, Hill C, Marshall J (2002) Global ocean circulation during 1992–1997, estimated from ocean observations and a general circulation model. *J Geophys Res* 107(C9):3118. doi:[10.1029/2001JC000888](https://doi.org/10.1029/2001JC000888)
- von Storch H, Zwiers F (1999) Statistical analysis in climate research. Cambridge University Press
- Todd R, Rudnick D, Mazloff M, Davis R, Cornuelle B (2011) Poleward flows in the southern California Current System: Glider observations and numerical simulation. *J Geophys Res* 116:C02026. doi:[10.1029/2010JC006536](https://doi.org/10.1029/2010JC006536)
- Verdy A, Mazloff M, Cornuelle BD, Kim SY (2013) Wind-driven sea level variability on the California coast: An adjoint sensitivity analysis. *J Phys Oceanogr* 44(1):297–318. doi:[10.1175/JPO-D-13-018.1](https://doi.org/10.1175/JPO-D-13-018.1)
- Weisberg RH, Li Z, Muller-Karger R (2001) West Florida shelf response to local wind forcing: April 1998. *J Geophys Res* 106(C12):31,239–31,262. doi:[10.1029/2000JC000529](https://doi.org/10.1029/2000JC000529)
- Weller RA (1981) Observations of the velocity response to wind forcing in the upper ocean. *J Geophys Res* 86(C3):1969–1977. doi:[10.1029/JC086iC03p01969](https://doi.org/10.1029/JC086iC03p01969)
- Winant CD (2004) Three-dimensional wind-driven flow in an elongated rotating basin. *J Phys Oceanogr* 34:462–476
- Winant CD, Beardsley RC, Davis RE (1987) Moored wind, temperature, and current observations made during Coastal Ocean Dynamics Experiments 1 and 2 over the Northern California continental shelf and upper slope. *J Geophys Res* 92(C2):1569–1604. doi:[10.1029/JC092iC02p01569](https://doi.org/10.1029/JC092iC02p01569)
- Wunsch C (1996) The ocean circulation inverse problem. Cambridge University Press, NY
- Xing J, Davies A (2004) On the influence of a surface coastal front on near-inertial wind-induced internal wave generation. *J Geophys Res* 109(C1):C01023. doi:[10.1029/2003JC001794](https://doi.org/10.1029/2003JC001794)
- Yelland M, Taylor PK (1996) Wind stress measurements from the open ocean. *J Phys Oceanogr* 26:541–558
- Young IR (1999) Wind generated ocean waves, vol. 2. Elsevier, London
- Zhang X, Cornuelle B, Roemmich D (2011) Adjoint sensitivity of the Niño-3 surface temperature to wind forcing. *J Clim* 24:4480–4493. doi:[10.1175/2011JCLI3917.1](https://doi.org/10.1175/2011JCLI3917.1)